The mineralization of the Woxi Au-Sb-W deposit, western Hunan, China

By:

Yi LIANG

Department of Earth and Planetary Systems Science

Graduate School of Science

Hiroshima University

Hiroshima, Japan, 2015

A thesis submitted to the School of Graduate Studies and Research in partial fulfillment of the requirements for the degree of Doctor of Philosophy at the University of Hiroshima

Contents

The main thesis:

Yi Liang, 2015. The mineralization of the Woxi Au-Sb-W deposit, western Hunan, China

Published papers:

1. Yi Liang and Kenichi Hoshino, 2015. Thermodynamic calculations of Au_xAg_{1-x}-fluid equilibria and their applications for ore-forming conditions. Applied Geochemistry, Vol. 52, 109-117.

2. Yi Liang, Guogang Wang, Shengyou Liu, Yuzhen Sun, Yonggang Huang and Kenichi Hoshino, 2015. A Study on the Mineralization of the Woxi Au–Sb–W Deposit, Western Hunan, China. Resource Geology, Vol. 65, 27-38.

The main thesis

Table of Contents

Abstract 1

1. Introduction 3

2. Geological setting 5

2.1 Regional geology 5

2.2 Local geology 6

3. Mineralization 12

3.1 Ore veins 12

3.2 Minerals 12

3.2.1 Stibnite, scheelite and native gold 12

3.2.2 Other minerals 13

3.3 Mineralogical sequence 14

4. Analyses and results 20

4.1 Chemical compositions of native gold and pyrite 20

4.2 Microthermometric analyses of fluid inclusions 21

4.3 LA-ICP-MS analyses of fluid inclusions 22

5. Thermodynamic calculations of Au_xAg_{1-x} - fluid equilibria 31

5.1 Introduction 31

5.2 Model calculations 32

5.3 Results 33

6. Discussion 64

6.1 Native gold mineralization 64

6.2 Ore-forming fluids and related mineralizations 65

7. Conclusion 67

Acknowledgments 69

References 70

Abstract

The Woxi Au-Sb-W deposit in the western Hunan Province, China, is of hydrothermal vein type characterized by a rare mineral assemblage of stibnite, scheelite and native gold of which gold fineness ranges from 998.6 to 1000. The mineralization sequence observed in the deposit is, from early to late, coarse-grained pyrite – scheelite – stibnite – Pb-Sb-S minerals – sphalerite (+ cubanite) – fine-grained pyrite. Native gold might have precipitated with scheelte.

Microthermometric and LA-ICP-MS analyses of fluid inclusions in scheelite, quartz associated with scheelite and stibnite and barren quartz clarified that there might be at least three types of hydrothermal fluids during the vein formation in the Woxi deposit. Scheelite and native gold precipitated from the fluid of high temperature and salinity with high concentrations of metal elements, followed by stibnite precipitation. The later fluid of the highest temperature and salinity with low concentrations of the elements yielded the sphalerite mineralization. The latest fluid of low temperature and salinity with low concentrations of the elements is observed mainly in barren quartz. The remarkably high Au/Ag concentration ratios determined in the fluid inclusions in scheelite might be the reason for the extremely high gold fineness of native gold.

Concentrations of dissolved gold and silver species in hydrothermal fluids equilibrated with Au-Ag solid solutions have been calculated at wide conditions

on the well known fO_2-pH spaces. Ratios of the total concentrations of dissolved gold and silver species ($\sum$Au/$\sum$Ag) are higher as pH higher and fO_2 lower. The ratios are constant at very low and high pH conditions where major dissolved species of both gold and silver are chloride complexes and thio complexes, respectively, while the ratios practically depend only on pH at intermediate pH conditions where $Au(HS)_2^-$ and $AgCl_2^-$ are major. The calculated results indicate that the solid solutions of high gold finenesses may precipitate from the fluids of low ratios of the total concentrations of dissolved gold and silver species when the conditions are (1) low pH's and/or (2) high concentration ratios of dissolved chlorine and sulfur and/or (3) high temperatures.

Compositional data of the fluid inclusions in scheelite from the Woxi deposit indicate that the extremely high gold finenesses of the native gold in the deposit might be caused by high Au/Ag concentration ratios and high temperatures of the ore-forming fluids.

1. Introduction

There are more than 100 Au-Sb (-W) deposits found in low-grade metamorphic rocks of the Proterozoic age in the western Hunan Province, China. The total proved ore reserves are 0.25 Mt WO_3, 1.67 Mt Sb and 42 t Au (Luo et al., 1996), with average grades ranging from 0.2% to 0.8% WO_3, 2% to 6% Sb and 5 to 10 g/t Au (Gu et al., 2007). Yang and Blum (1999b) pointed that most of the above deposits occur in a specific horizon of the Proterozoic Madiyi Formation.

The Woxi Au-Sb-W deposit, the largest one hosted in the Madiyi Formation, represents one of few documented cases where W, Sb, and Au mineralization occur within a large-scaled single deposit (Gu et al., 2007). Stibnite is the largest ore reserve in the Woxi deposit. Productions of refined antimony and oxide antimony were about 40,000 tons in 2010 (from the mine data). Scheelite is the second one from which tungstate was produced about 5,000 tons in 2010. The gold production of the deposit in 2010 was about 2 tons, the largest one of Hunan Province.

The Woxi deposit has been conceived as a hydrothermal vein type (Yang and Blum, 1999a). However, due to its complex mineralization, detailed mineral parageneses and characteristics of ore-forming fluids, as well as the mineralization mechanism are still in debate in the previous studies.

This thesis presents the geological setting of the Woxi deposit, results of microscopic observations and EPMA analyses of minerals, as well as microthermometic and LA-ICP-MS analyses of fluid inclusions. Solubilities of

the Au-Ag solid solutions have also been analyzed theoretically in the present study. Based on those observations and analytical results, characteristics of ore-forming fluids of the Woxi deposit are discussed.

2. Geological setting

2.1 Regional geology

It is well known that South China consists of two complex terranes, the Yangtze Craton to the northwest and the Cathaysia Block to the southeast (Figure 2.1). The collision between the Yangtze Craton and the Cathaysia Block occurred during middle-late Proterozoic times and led to uplift of the Jiangnan orogenic belt (Gu et al., 2007). The Woxi Au-Sb-W deposit is located in the western segment of the Jiangnan orogenic belt (Gu et al., 2007) in the northwest Hunan region approximately 200 kilometers west of the capital city of Hunan Province, Changsha.

In South China, a structural deformation event of the Yanshan movement is marked by wide magmatic activities. However, the magmatic activity around the Woxi deposit is scarce, and the nearest igneous intrusive is about 50 kilometers southeast from the deposit. Lithologic units of the northwestern Hunan region mainly consist of low grade metamorphic rocks of the Proterozoic age (Yang and Blum, 1999a) which is divided into two stratigraphic groups: the Lengjiaxi Group and the Banxi Group (Figure 2.2a). The former is widely distributed (Peng and Frei, 2004) and shows ages between 1566 Ma and 1157 Ma (Rb-Sr on whole rocks; Tang et al., 1994). While the later, which might be deposited under shallow marine conditions, comprises the Madiyi Formation and the Wuqiangxi Formation (Yang and Blum, 1999a). Sedimentation ages of the Madiyi Formation were estimated between 933 Ma

and 855 Ma (Tang et al., 1994), while the Wuqiangxi Formation was dated by a U-Pb zircon age as 746 Ma (Gan, 1996). It was noted by Yang and Blum (1999a) that the Banxi Group is the main lithological horizon for the metal deposits (Figure 2.2b). Yang and Blum (1999b) pointed that there is a large-scaled uplift zone with alt basement in the northwestern Hunan Province (Figure 2.2c). There are more than 40 Au-Sb (-W) deposits located in the uplift zone, of which 80% are hosted in the Madiyi Formation, while 20% are in the Wuqiangxi Formation (Yang and Blum, 1999a).

2.2 Local geology

In the Woxi mining district, lithological units include the Cretaceous formation (reddish conglomerates) and the Madiyi and Wuquiangxi Formations of the Proterozoic Banxi Group (Figure 2.2a). Rocks in the Madiyi Formation are red-black colored sericite-bearing slates and gray-white colored silicified ones as well as interbedded sandstones, while the Wuquiangxi Formations consists of gray-green colored sandy slates, arkoses and sandstones. The Woxi fault occurs at the boundary between the Wuqiangxi Formation and the Madiyi Formation with its length of about 15 kilometers (Figure 2.2a). A number of minor faults also occur in the district (Figure 2.3), commonly cutting ore veins. Many small-scaled folding structures are observed in the vicinity of the Woxi mining district, which might have deformed the ore veins (Figure 2.2a).

A large number of quartz veins occur mainly in the silicified slates of the Madiyi Formation in the Woxi deposit. The ore mineralization is found mostly in the quartz veins, while rare in the host slates. The Wuqiangxi Formation is underlain by the Madiyi Formation with rare mineralization and small quartz veinlets.

Pyrite and sericite are observed as later alteration products in the ore veins, while hydrothermal bleaching and carbonatization can be identified around the veins. The pyritization has been thought as an important indicator for the gold mineralization, as well as the other alterations for hydrothermal activities in the mining area (Yang and Blum, 1999a).

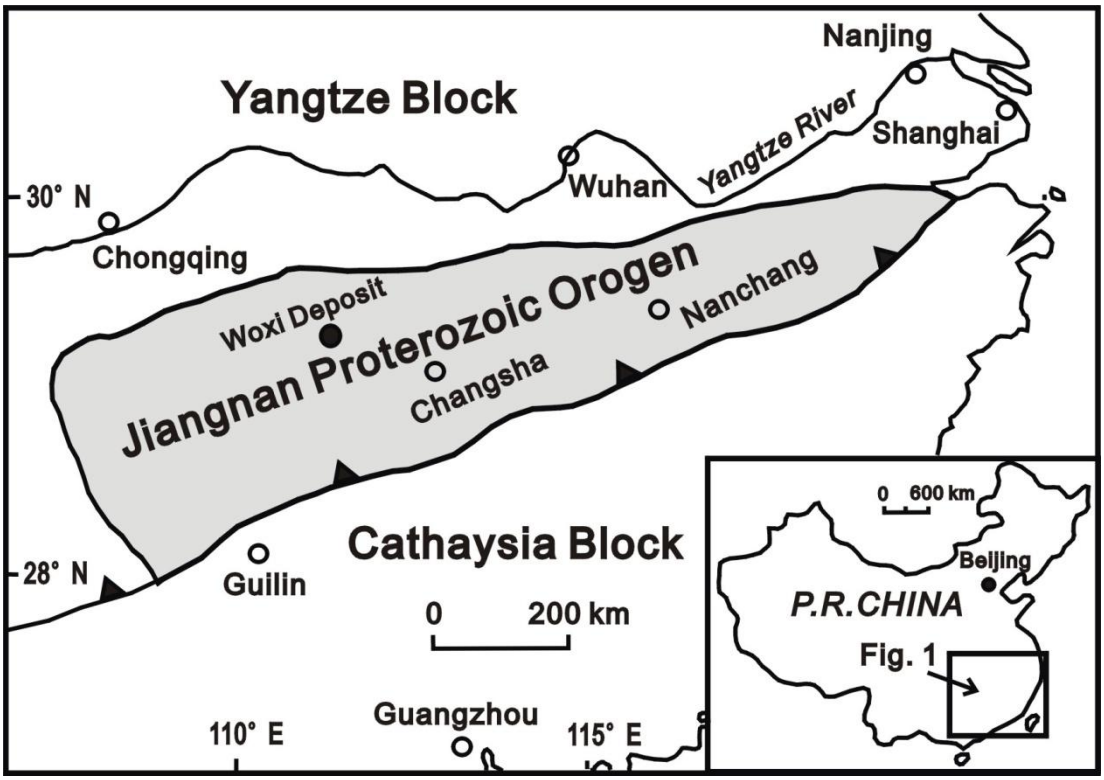

Figure 2.1. A tectonic map of South China with the location of the Woxi deposit (modified from Gu et al., 2007).

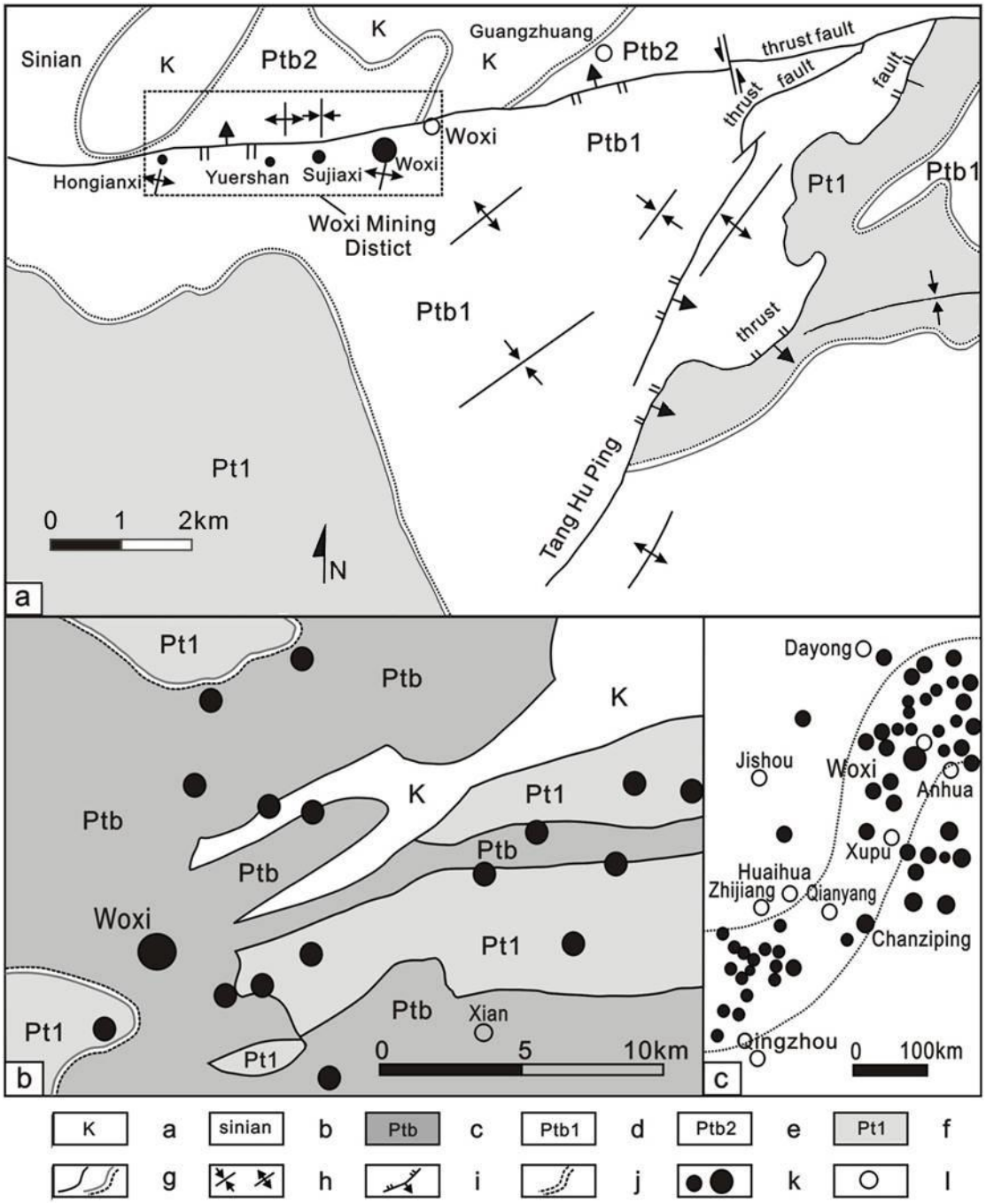

Figure 2.2. Geological maps around the Woxi deposit (modified from Yang and Blum, 1999a). (a) The geological map in the region of the Woxi deposit. (b) The sketch map of deposits in northwestern Hunan province. (c) The regional map of deposits in the vicinity of the Woxi deposit. Legend: a = Cretaceous red

sandy conglomerate; b = Sinian; c = Banxi Group (Neoproterozoic); d = Madiyi Formation (Banxi Group); e = Wuquangxi Formation (Banxi Group); f = Lengjiaxi Formation (Neoproterozoic); g = strata boundary line and discordant plane; h = anticline and syncline; i= thrust fault; j = uplift zone with alt basement; k = deposits (large black circles stand for large deposits, middle (small) black circles for middle (small) deposits or ore mineralization); l = town.

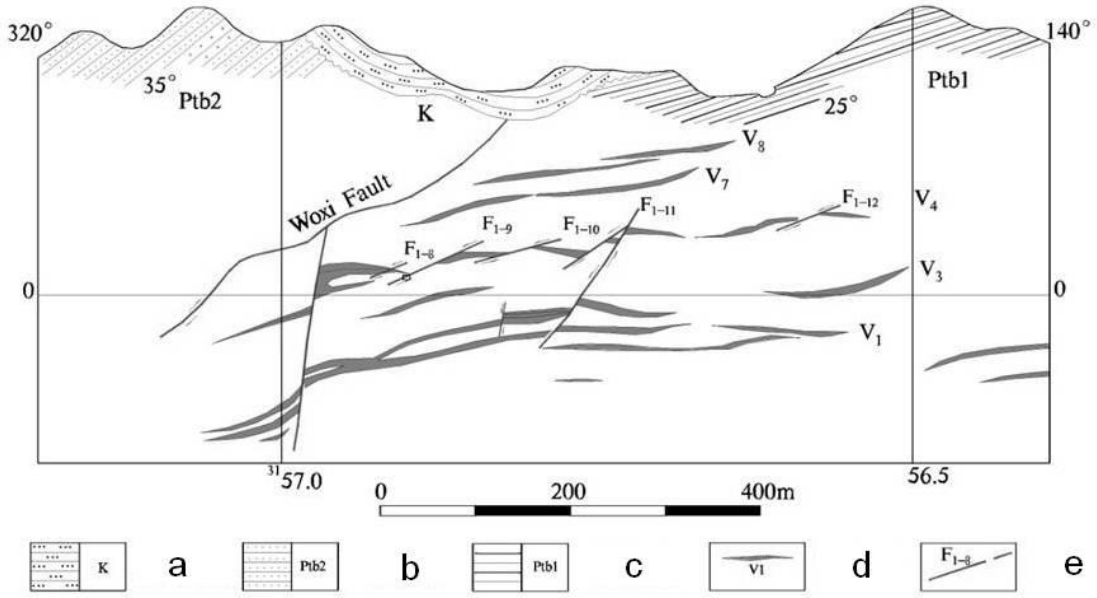

Figure 2.3. A geological section map around the Woxi deposit (modified from the mining data). Legend: a = Cretaceous reddish conglomerates; b = Wuqiangxi Formation sandy slates; c = Madiyi Formation silicified slates; d = Ore veins and their numbers; e = Faults.

3. Mineralization

3.1 Ore veins

There are 8 major quartz veins in the Woxi deposit. The veins, V_1, V_3, V_4, V_7 and V_8 are called as ore veins with high ore grades of stibnite, scheelite and native gold (Figure 3.1). As can be seen in Figure 2.3, the veins are cut by many small faults. For example, the V_4 ore vein is cut into several sections by six small faults.

Average thicknesses of ore veins ranging from 0.72m to 1.51m generally show a negative correlation with their average ore grades of Sb, W and Au (Figure 3.2). On the other hand, the variation in average ore grades of Sb and W show the same tendency with each other in different ore veins, while that of Au is different from others (Figure 3.2).

3.2 Minerals

3.2.1 Stibnite, scheelite and native gold

Stibnite shows subhedral or anhedral in shape (Figure 3.3a). Microscopic observations of ore samples revealed that aggregates of subhedral stibnite are commonly associated with quartz and cut by later thin quartz veinlets (Figure 3.3j) and sphalerite veinlets (Figure 3.3k), while anhedral stibnite commonly fills fractures of coarse-grained pyrite (Figure 3.3i) and scheelite crystals (Figure 3.3d). The above observations indicate that stibnite precipitated after

the coarse-grained pyrite and scheelite, but before sphalerite and the thin quartz veinlets.

Milky white colored scheelite is found in the large quartz veins. It occurs as euhedral or aggregates of subhedral crystals (Figure 3.3c). The aggregates are often cut by the later thin quartz veinlets including fine-grained pyrite (Figure 3.3e). Fractures of euhedral scheelite are also filled by the later small quartz veinlets and stibnite (Figure 3.3d). On the other hand, a lot of scheelite crystals are found in fractures of coarse-grained pyrite (Figure 3.3f). Those modes of occurrence of scheelite and stibnite suggest that scheelite precipitated after the coarse-grained pyrite, but before stibnite, the thin quartz veinlets and the fine-grained pyrite.

A small amount of fine-grained native gold is found in stibnite with quartz (Figure 3.3g), while a large amount of coarse-grained native gold can be observed as fillings in microfactures of the coarse-grained pyrite crystals (Figure 3.3h and i), implying that native gold precipitated after the coarse-grained pyrite.

3.2.2 Other minerals

Two types of pyrite are observed in the ore veins. The one is fine-grained (0.02mm-0.1mm) and commonly found in the thin quartz veinlets (Figure 3.3e and j), while the other is coarse-grained (0.1mm-5mm) of which microfractures are filled by scheelite (Figure 3.3f), stibnite (Figure 3.3h and i), native gold

(Figure 3.3i) and sphalerite (Figure 3.3n). Therefore, it could be concluded that the coarse-grained pyrite precipitated earlier than the fine-grained one.

Sphalerite associated with cubanite (Figure 3.3m, determined by EPMA) is found in one sample from the V_4 ore vein cut by several faults. The following modes of occurrence of sphalerite could be observed under microscope, coarse-grained sphalerite disseminated by the fine-grained pyrite (Figure 3.3l), sphalerite filling fractures of the coarse-grained pyrites (Figure 3.3n) and sphalerite veinlets in stibnite (Figure 3.3k). Hence, sphalerite might have precipitated after the coarse-grained pyrite and stibnite, but before the fine-grained pyrite.

Two Pb-Sb-S minerals, zinkenite ($Pb_6Sb_{14}S_{27}$) and plagionite ($Pb_5Sb_8S_{17}$) are identified by EPMA analyses. Zinkenite is cut by the thin quartz veinlet (Figure 3.3o), indicating its precipitation stage before the veinlet. Plagionite fills fractures of the coarse-grained pyrite with sphalerite (Figure 3.3n). Since a part of plagionite veinlet is occupied by sphalerite, plagionite might have precipitated slightly earlier than sphalerite.

3.3 Mineralogical sequence

Minerals observed in the Woxi deposit are mainly scheelite, stibnite, native gold, pyrite and quartz with minor amounts of sphalerite, cubanite and Pb-Sb-S minerals. Detailed microscopic observations described in the above section reveal the mineralogical sequence in the deposit as, from early to late, coarse-grained pyrite – scheelite – stibnite – Pb-Sb-S minerals – sphalerite (+

cubanite) – fine-grained pyrite. Although native gold precipitated later than the coarse-grained pyrite, a certain stage of gold mineralization could not be confirmed by microscopic observations.

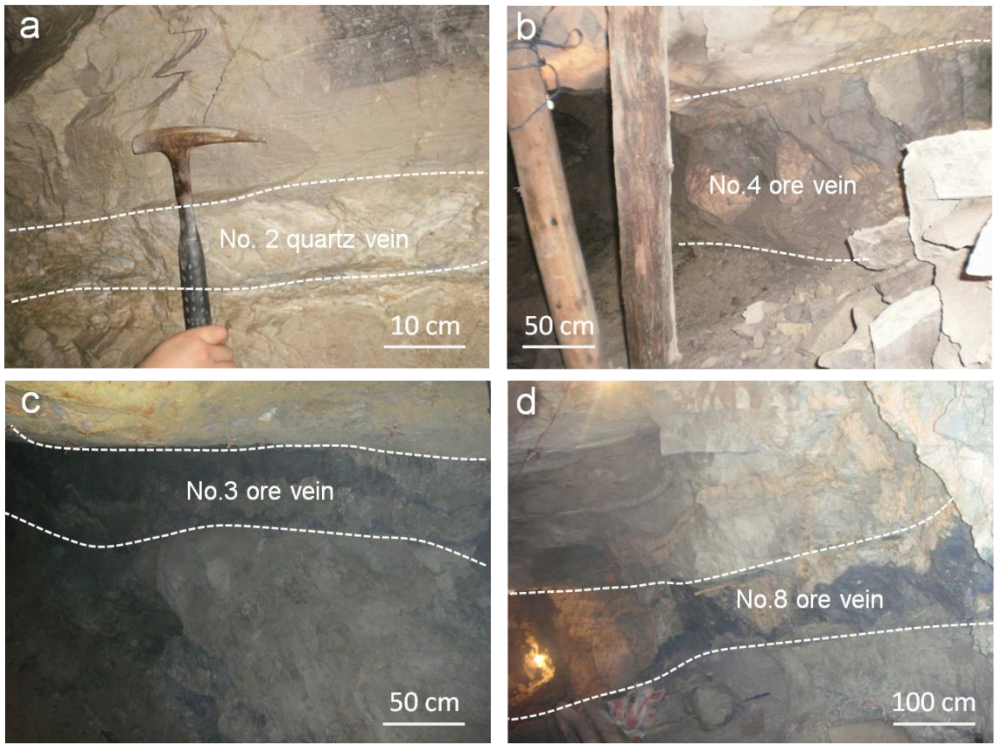

Figure 3.1. Photographs showing a quartz vein and three ore veins in the Woxi deposit (Liang et al., 2015). (a): No.2 quartz vein; (b): No.4 ore vein; (c): No.3 ore vein (d): No.8ore vein.

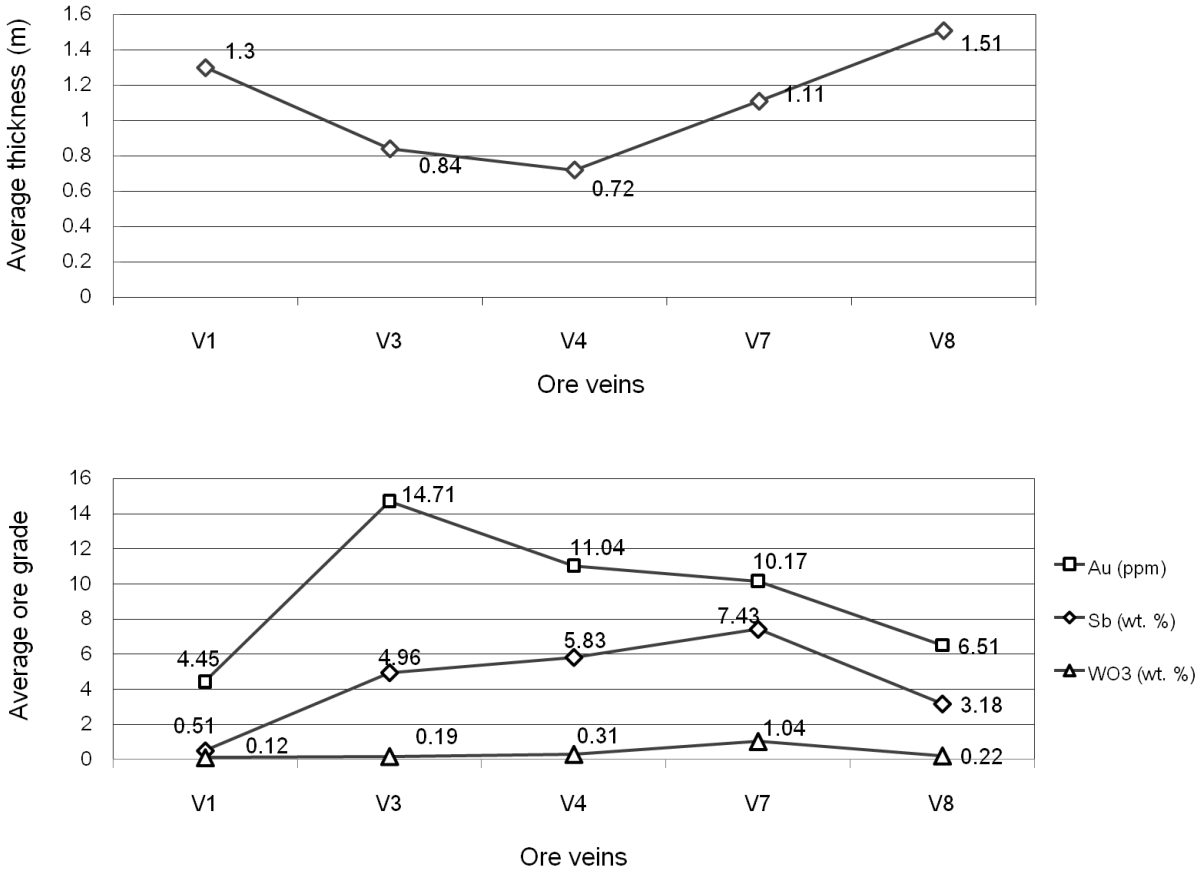

Figure 3.2. Diagrams showing average thicknesses (top) and average ore grades (bottom) of ore veins (modified from the mining data).

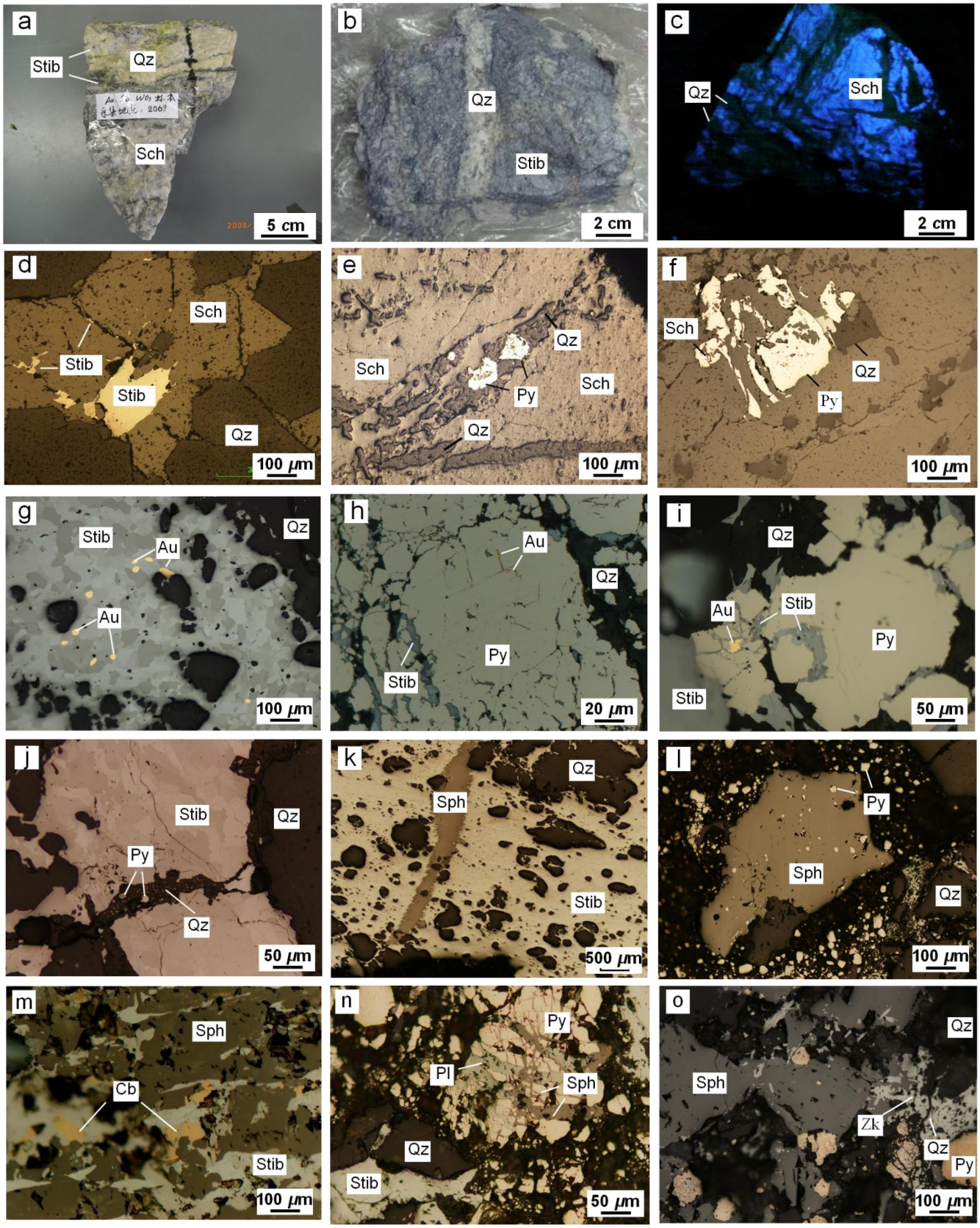
a
Stib
Qz
Sch
5 cm
b
Qz
Stib
2 cm
c
Qz
Sch
2 cm
d
Sch
Stib
Stib
Qz
100 μm
e
Qz
Sch
Py
Sch
Qz
100 μm
f
Sch
Qz
Py
100 μm
g
Stib
Au
Qz
Au
100 μm
h
Au
Qz
Py
Stib
20 μm
i
Qz
Au
Stib
Py
Stib
50 μm
j
Stib
Qz
Py
Qz
50 μm
k
Qz
Sph
Stib
500 μm
l
Py
Sph
Qz
100 μm
m
Sph
Cb
Stib
100 μm
n
Py
Pl
Sph
Qz
Stib
50 μm
o
Qz
Sph
Zk
Qz
Py
100 μm

Figure 3.3. Photographs and photomicrographs of ores from the Woxi deposit (Liang et al., 2015). Abbreviations: Stib: stibnite; Sch: scheelite; Au: native gold; Qz: quartz; Py: pyrite; Sph: sphalerite; Cb: cubanite; Pl: plagionite; Zk: zinkenite.

4. Analyses and results

4.1 Chemical compositions of native gold and pyrite

Nineteen points on native gold grains with various modes of occurrences are analyzed by EPMA (JEOL JXA-8200) at Hiroshima University with an acceleration voltage and a probe current of 20 kV and 1.0×10^{-8} A, respectively. Since only gold and silver are detected in native gold, the gold fineness, a term in metallurgy defined by,

$$\text{Gold fineness} = \text{Au (wt. \%)} / [\text{Au (wt. \%)} + \text{Ag (wt. \%)}] \times 1000,$$

will be taken to present the chemical compositions of native gold from the Woxi deposit hereafter.

The all analyzed points show remarkably high gold finenesses ranging from 998.6 to 1000 (Table 4.1). It should be noted that such a super pure gold is rarely reported in the previous studies of hydrothermal deposits.

EPMA analyses of pyrite revealed that arsenic concentrations in pyrite range from 0 to 2.9 wt. % (Table 4.2). It is interesting that the early coarse-grained pyrite associated with quartz, stibnite and scheelite contains As higher than 0.3 wt. %, while the later fine-grained pyrite in the quartz veinlets shows lower compositions (0 - 0.3 wt. %).

4.2 Microthermometric analyses of fluid inclusions

Fluid inclusions hosted in quartz, shceelite and sphalerite have been analyzed microthermometrically by the Linkam L-600K. The melting temperature of frozen pure water was checked before analyses with a heating rate of 2 °C/min. Fluid inclusions are heated at a rate of 5 °C/min when they are close to being homogenized. A homogenization temperature of each fluid inclusion was measured twice and confirmed the difference within 5℃. Homogenization temperatures in barren quartz are 120-320°C, while those in quartz with stibnite and in quartz with scheelite are 120-340°C and 140-400°C, respectively (Figure 4.1). The temperatures of the inclusions in scheelite and in sphalerite are 120-400°C and 260-440°C, respectively (Figure 4.1). Although the temperatures show wide ranges, the histogram in Figure 4.1 likely indicates the bimodal distribution with peaks at around 200°C and 300℃, implying that one mode showing temperatures of an earlier fluid overprinted by another mode of a later one. It is also seen in the figure that the fluid inclusions in sphalerite and scheelite tend to show relatively higher homogenization temperatures than those in quartz.

As compare to the homogenization temperatures, salinities of the fluid inclusions estimated from melting temperatures of frozen liquid phases show a distinct difference between those in scheelite and sphalerite and those in quartz with stibnite and barren quartz (Figure 4.2). The former show higher salinities (5-10 wt. % NaCl eq.), while the later are lower (1-6 wt. % NaCl eq.).

By comparing those results with the mineralogical sequence determined in the previous section, it may be said that the temperatures and salinities of fluid during the scheelite mineralization were higher than those during the stibnite mineralization with quartz and that a later fluid with the highest temperature and salinity might have precipitated sphalerite.

4.3 LA-ICP-MS analyses of fluid inclusions

LA-ICP-MS analyses were taken for 24 fluid inclusions in various host minerals. Types of a laser and an ICP-MS used in the analyses are VG PQ-3 and UP-213, respectively. Analyzed elements are ^{7}Li, ^{23}Na, ^{39}K, ^{42}Ca, ^{55}Mn, ^{57}Fe, ^{65}Cu, ^{66}Zn, ^{75}As, ^{85}Rb, ^{95}Mo, ^{107}Ag, ^{118}Sn, ^{121}Sb, ^{133}Cs, ^{182}W, ^{197}Au, ^{208}Pb and ^{209}Bi. The accuracy and precision of analytical data were calibrated by following the procedures presented by Heinrich et al. (2003) with the standard of NIST glass (NIST SRM 610). The indicative limitations of detection for elements in fluid inclusion analyses (used in Table 4.3) proposed by Heinrich et al. (2003) are much higher than the detection limits of the instrument.

The analytical results show that all fluid inclusions in scheelite are rich in the metal elements (Table 4.3). It is also worth noting that high Au concentrations are determined only in the fluid inclusions in scheelite (Figure 4.3a), whereas those in the other minerals show very low concentrations.

The results also revealed that four inclusions showing higher homogenization temperatures and salinities in quartz with stibnite and scheelite are also rich in the metal elements, whereas the other three

inclusions of lower homogenization temperatures and salinities are poor in them. It can be seen in Figure 4.3b that an Sb concentration in the fluid inclusion in quartz with stibnite is clearly high, indicating that the fluid precipitating stibnite was certainly trapped in quartz coexisting with stibnite.

Only one fluid inclusion of high homogenization temperature and salinity in sphalerite could be analyzed and shows low concentrations of the metal elements (Figure 4.3c).

Fluid inclusions in barren quartz are poor in the metal element (Figure 4.3d) except the one showing the highest homogenization temperature.

Table 4.1. EPMA analyses of native gold from the Woxi deposit and their gold finenesses (Liang et al., 2015).

Mode of occurrence	Vein	Au (wt. %)	Ag (wt. %)	Gold fineness
in pyrite	No.4	99.86	0.14	998.6
in pyrite	No.4	99.90	0.10	998.9
in pyrite+stibnite	No.7	99.92	0.08	999.2
in pyrite+stibnite	No.7	99.88	0.12	998.8
in pyrite+stibnite	No.7	99.90	0.10	998.9
in pyrite+stibnite	No.4	99.89	0.11	998.9
in pyrite+stibnite	No.8	99.87	0.13	998.7
in pyrite+stibnite	No.7	99.92	0.08	999.2
in stibnite	No.8	99.90	0.10	999.1
in stibnite	No.8	99.89	0.11	998.9
in stibnite	No.8	99.88	0.12	998.8
in stibnite	No.8	99.90	0.10	999.1
in quartz+stibnite	No.4	99.94	0.08	999.4
in quartz+stibnite	No.8	99.99	0.01	999.9
in quartz+stibnite	No.8	100.00	0.00	1000.0
in quartz+pyrite	No.7	100.00	0.00	1000.0
in quartz	No.4	100.00	0.00	1000.0
in quartz	No.8	100.00	0.00	1000.0
in quartz	No.4	100.00	0.00	1000.0

Table 4.2. EPMA analyses of pyrite from the Woxi deposit (Liang et al., 2015).

Mode of occurrence	Fe (wt. %)	S (wt. %)	As (wt. %)	Total
in quartz veinlet of stibnite	45.3	53.4	0.0	98.7
in quartz veinlet of stibnite	46.5	53.7	0.0	100.2
in quartz veinlet of stibnite	45.4	52.9	0.0	98.3
in quartz veinlet of stibnite	46.0	54.4	0.1	100.5
in quartz veinlet of scheelite	46.5	53.7	0.3	100.5
with sphalerite	43.8	52.3	0.3	96.4
with quartz and stibnite	46.2	53.3	0.4	99.9
with quartz and stibnite	46.2	53.5	0.5	100.2
with stibnite	46.4	52.7	0.9	100.0
with stibnite	45.8	53.3	1.0	100.1
with quartz and stibnite	46.5	53.3	1.1	100.9
with scheelite	46.2	52.8	1.3	100.3
with stibnite	45.6	52.2	1.3	99.1
with quartz and stibnite	45.4	52.3	1.8	99.5
with quartz and stibnite	45.2	51.7	2.2	99.1
with stibnite	45.3	50.9	2.9	99.1

Table 4.3. LA-ICP-MS analyses of fluid inclusions with their homogenization temperatures and salinities (Liang et al., 2015).

Vein	H.T (℃)	Salinity (wt. %)	Size (*u*m)	Na (wt. %)	K (wt. %)	Ca (wt. %)	Fe (wt. %)	Cu (ppm)	Zn (ppm)	As (ppm)	Rb (ppm)	Mo (ppm)	Ag (ppm)	Sn (ppm)	Sb (ppm)	W (ppm)	Au (ppm)	Pb (ppm)	Bi (ppm)
Host mineral: barren quartz																			
V1	212	3.2	10	1.3	–	–	–	–	43	–	–	–	–	–	11	–	–	–	–
V7	178	3.1	10	1.2	–	–	–	–	–	–	–	–	–	–	–	–	–	–	–
V7	205	6.4	10	0.2	0.11	4.1	–	–	–	–	–	–	–	–	23	28	–	–	–
V7	210	1.6	20	0.6	–	–	–	–	–	+	–	–	–	–	435	-	–	–	–
V7	214	1.6	25	0.6	–	–	–	–	–	+	–	–	–	–	336	59	–	–	–
V7	214	2.1	15	0.8	–	–	–	–	–	+	–	–	–	–	183	–	–	–	–
V7	213	4.8	15	1.3	–	–	0	–	–	+	–	–	–	–	30	–	–	–	–
V7	225	5.1	10	1.8	–	–	0	–	–	+	–	–	–	–	19	8	–	–	–
V7	222	4	15	1.2	–	–	0	–	–	+	–	–	–	–	75	32	–	–	–
V7	232	4.6	15	1.9	–	–	0	–	13	–	–	–	–	–	–	–	–	–	–
V7	297	1.7	15	0.7	–	–	0	–	6	–	–	–	111	–	–	239	–	–	–
V7	308	3.2	15	0.7	0.02	0.8	0.36	101	192	–	–	92	–	7	491	39	–	374	–
Host mineral: sphalerite																			
V4	280	9.3	25	3.7	–	–	–	–	omit	–	–	–	–	–	–	–	–	–	–

Table 4.3. (continued)

Vein	H.T (℃)	Salinity (wt. %)	Size (*u*m)	Na (wt. %)	K (wt. %)	Ca (wt. %)	Fe (wt. %)	Cu (ppm)	Zn (ppm)	As (ppm)	Rb (ppm)	Mo (ppm)	Ag (ppm)	Sn (ppm)	Sb (ppm)	W (ppm)	Au (ppm)	Pb (ppm)	Bi (ppm)
Host mineral: quartz with stibnite and scheelite																			
V3	200	4.3	15	1.7	–	–	–	–	–	–	–	–	–	–	202	–	–	–	–
V3	220	3.9	15	1.1	–	–	–	–	–	–	–	–	–	–	242	–	–	–	–
V3	198	3.4	15	1.2	–	–	–	–	–	–	–	–	–	–	335	11	–	–	–
V7	338	7	30	2.1	1.1	–	0.13	233	152	+	–	22	229	32	5302	19	–	558	11
V7	237	6.3	25	2.1	0.8	–	0.19	268	215	+	27	16	435	22	760	63	–	35	–
V7	313	7	15	2.6	0.2	–	0.32	82	208	+	43	22	37	58	omit	40	–	635	57
V7	334	3.1	20	1.1	0.3	–	0.1	241	165	+	12	83	1011	39	2619	41	–	90	–
Host mineral: scheelite																			
V7	198	4.3	15	1.3	0.05	omit	0.03	68	18	+	–	–	5	–	137	omit	11	40	–
V8	357	8.3	15	0.5	–	omit	5.8	48	687	+	24	11	18	9	946	omit	–	26	–
V8	303	6.7	10	2.5	0.32	omit	0.3	150	967	+	31	83	5	17	569	omit	18	128	–
V8	356	5.8	15	1.8	0.07	omit	0.8	23	212	+	–	20	8	11	246	omit	24	124	–

H.T.: homogenization temperature; –: lower than the indicative limitation of detection (LOD, proposed by Heinrich et al. (2003)); +: arsenic showing high intensity peaks; omit: the intensity is too high to calculate the absolute concentration.

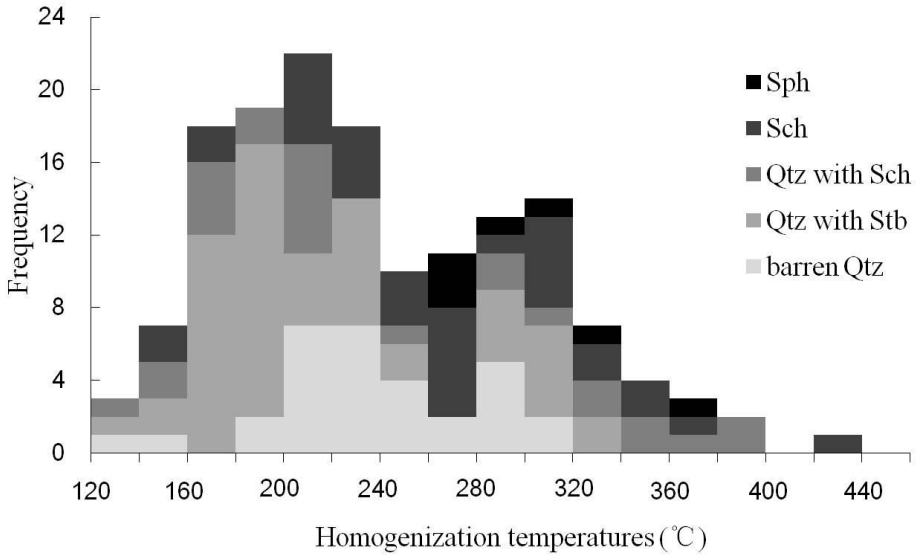

Figure 4.1. Homogenization temperatures of fluid inclusions (Liang et al., 2015). Sph: in sphalerite; Sch: in scheeite; Qtz with Sch: in quartz coexisting with shceelite; Qtz with Stb: in quartz coexisting with stibnite; barren Qtz: in barren quartz.

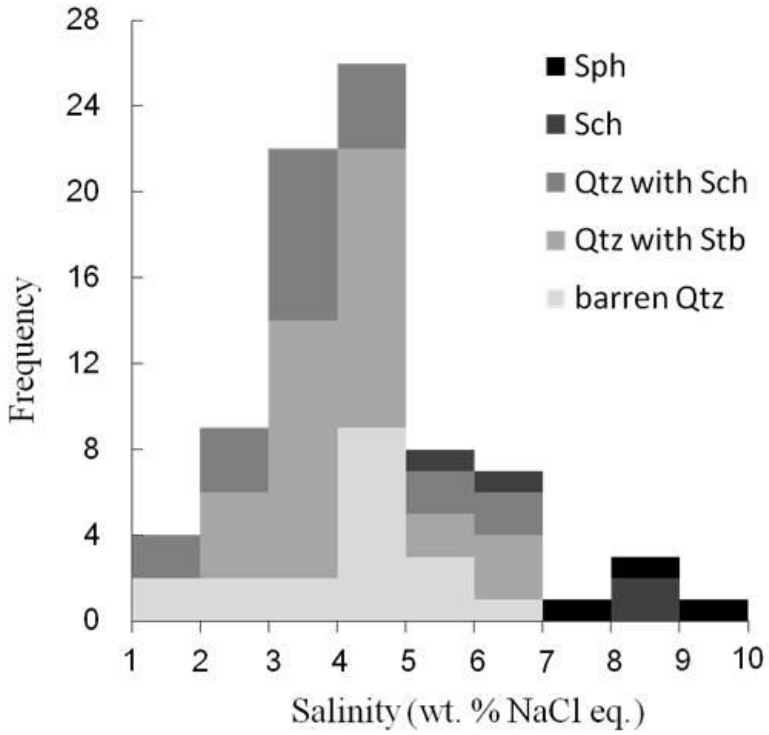

Figure 4.2. Salinities of fluid inclusions (Liang et al., 2015). See Figure 4.1 for abbreviations.

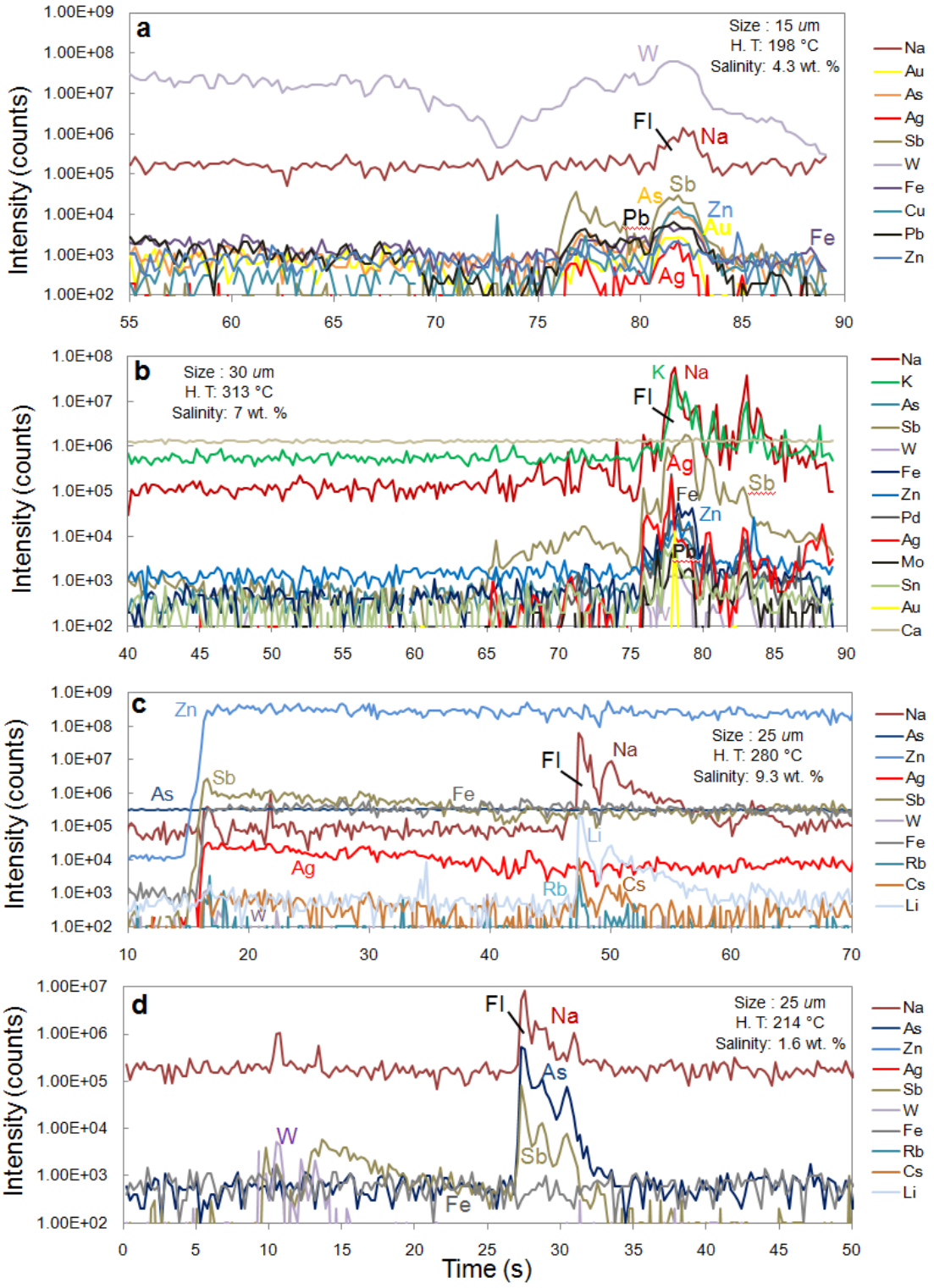

Figure 4.3. Transient signal data for fluid inclusions generated by LA-ICP-MS (Liang et al., 2015). (a): in scheelite; (b): in quartz with stibnite; (c): in sphalerite; (d): in barren quartz.

5. Thermodynamic calculations of Au_xAg_{1-x} - fluid equilibria

5.1 Introduction

Au-Ag solid solutions are characterized by a wide variation in chemical compositions commonly expressed as the gold fineness (1000×Au/(Au+Ag), by weight) (e.g., Fisher,1945; Morrison et al., 1991; Pal'yanova, 2008). Three minerals are defined by the fineness as native gold (the fineness greater than 800), electrum (between 200 and 800) and native silver (less than 200) (Shikazono and Shimizu, 1987; Morrison et al., 1991).

A theoretical study of the Au-Ag solid solutions was commenced by White et al. (1957) who reported thermodynamic properties of Au-Ag solid solutions. Shikazono and Shimizu (1987), Spycher and Reed (1989), Krupp and Weiser (1992), Huston et al. (1992) and Gammons and Williams-Jones (1995), stressed the importance of Au-Ag solid solutions and developed generalized thermodynamic approaches describing co-precipitation of Au and Ag in natural hydrothermal systems (Pal'yanova, 2008). Pal'yanova (2008) successfully examined the detailed physicochemical conditions for equilibria of the Au-Ag solid solutions and fluids by taking account of recently determined thermodynamic data for mono ligands of gold and silver with other known species.

On the other hand, Au-Ag solid solutions of high gold finenesses have been reported from various types of Au-Ag deposits (e. g., Shikazono and Shimizu,

1987; Morrison et al., 1991), although most of reasons for high gold finenesses have not yet been clarified. Therefore, I have calculated solubilities of the solid solutions in wide conditions on the well known fO_2-pH diagrams to investigate controlling factors of gold finenesses. I have also summarized published data of 47 Au-Ag deposits including ranges of gold finenesses and ore-forming conditions (Table 5.1) to compare with results of my calculations.

5.2 Model calculations

Sixteen aqueous species of gold and silver counted in my calculations are listed in Table 5.2. Thermodynamic data of the species of AuHS, AuOH and AgHS are taken from Pal'yanova and Kolonin (2007), while those of other aqueous, gaseous and solid (gold, silver and acanthite/argentite) species are derived by SUPCRT92 (Johnson et al., 1992). Parameters of the Maier-Kelley equation for heat capacity of petrovskaite (AgAuS) was estimated by fitting the data listed in Gurevich et al. (2011). The parameters and other thermodynamic functions of petrovskaite estimated by them and those for uytenbogaardtite (Ag_3AuS_2) listed in Tagirov et al. (2006) with their molar volumes calculated from their densities in Pal'yanova and Savva (2008) are taken into the SUPCRT92 data set (Table 5.3).

Pal'yanova (2008) introduced the mixing model of the Au-Ag solid solution proposed by White et al. (1957) in his calculations as:

$$\ln \gamma_{Au} = (-4850 + 1600X + 1.375T)(1 - X)^2 / RT,$$

$$\ln \gamma_{Ag} = (-5650 + 1600X + 1.375T) X^2 / RT,$$

where γ_{Au} and γ_{Ag} are the activity coefficients of Au and Ag components in the solid solutions, respectively, X is the mole fraction of Au, R is the gas constant in cal/mol and T is temperature in K. However, I simply assumed an ideal mixing model with its site mixing parameter as unity for simplifying calculations. I believe that this simplification does not violate the following conclusions since the difference in logK of the reaction:

$$Au_XAg_{1-X} + H^+ + 1/4O_{2(aq)} = XAu^+ + (1-X)Ag^+ + 1/2H_2O$$

of the both models is small for the solid solutions with a high or low gold fineness (Figure 5.1) of which formation conditions I will discuss in the following sections. Activity coefficients of all dissolved species are taken as unity in the calculations.

Simultaneous equations for equilibria of all dissolved species with the Au-Ag solid solution of a fixed composition under certain pressure and temperature conditions are solved by using Mathematica (Wolfram, 1991).

5.3 Results

As is noted in the previous section, Pal'yanova (2008) successfully examined the detailed physicochemical conditions for equilibria of Au-Ag solid solutions and fluids. However, her analyses were focused mainly on the conditions of certain buffer assemblages of minerals of the Fe-S-O system such as pyrite-pyrrhotite (-magnetite). Therefore, results of my thermodynamic calculations are depicted on logfO_2-pH diagrams widely referred in studies of ore deposits with stability fields of those minerals.

5.3.1 Ratios of total concentrations of dissolved gold and silver

Solubilities of pure gold and silver in hydrothermal fluids have been well investigated in the previous studies (e. g., Hayashi and Ohmoto, 1991, Gammons and Barnes, 1989). Hence, I examined ratios of total concentrations of dissolved gold and silver ($R = \log(\sum Au/\sum Ag)$) in fluids equilibrated with the Au-Ag solid solutions of compositions of X_{Au} = 0.999 (gold fineness = 999, Figure 5.2a), 0.9 (gold fineness = 943, Figure 5.2b), 0.4 (gold fineness = 549, Figure 5.2c) and 0.001 (gold fineness = 2, Figure 5.2d) under the condition of P = 100 MPa and T = 300°C with the total dissolved chlorine and sulfur of 1 mol/kg and 0.01 mol/kg, respectively.

The chloride complexes of gold and silver are dominant at high fO_2 and low pH fields, while the thio complexes are major at high pH conditions. It is worth noting that total concentrations of dissolved gold species are highest at around the conditions where HSO_4^-, H_2S and HS^- are equally dominant as dissolved sulfur species, while those of silver decrease with increasing pH in the all figures. In the all analyzed fluids equilibrated with the Au-Ag solid solutions, the ratios, Rs tend to high at high pH and/or low fO_2 conditions.

It is interesting that the ratios do not depend on pH nor fO_2 at very low pH (<2) conditions, since the contours of the total concentration profiles for the dissolved gold and silver species are parallel with each other. This is because the dominant dissolved species of gold and silver in the conditions are $AuCl_2^-$ and $AgCl_2^-$, respectively. The same is true for the conditions of

high pH (>7) and low fO_2 where HS^- is dominant and $Au(HS)_2^-$ and $Ag(HS)_2^-$ are the major species. While, on the other hand, the ratios practically depend only on pH ($3 < pH < 7$) in the conditions where H_2S is predominant due to the following reason. The major aqueous species of gold and silver in the conditions are $AuHS_{(aq)}$ and $AgCl_2^-$, respectively. Hence, the dissolution reactions of silver and gold in the solid solution can be written as,

$$Ag_{(ss)} + 2Cl^- + H^+ + 0.25O_{2(aq)} = AgCl_2^- + 0.5H_2O$$

$$Au_{(ss)} + H_2S_{(aq)} + 0.25O_{2(aq)} = AuHS_{(aq)} + 0.5H_2O,$$

respectively. Since the concentrations of Cl^- and H_2S can roughly be taken as constant in the conditions, the concentration ratio of $AuHS_{(aq)}/AgCl_2^-$ depends only on pH and the activity ratio of Au and Ag in the solid solution (Figure 5.3).

5.3.2 Other dependencies of the concentration ratios

Dependencies of the ratios, Rs in the fluids equilibrated with the Au-Ag solid solutions of $X_{Au} = 0.9$ on temperature and pressure have been calculated at the fixed fO_2 (pyrite – pyrrhotite buffer at low pH) (Figure 5.4). By comparing Figs. 3 and 4, it can generally be said that the ratios do not depend on pH at low pH conditions where gold and silver dissolve mainly as $AuCl_2^-$ and $AgCl_2^-$, respectively, and at high pH where $Au(HS)_2^-$ and $Ag(HS)_2^-$ are dominant, while they increase with increasing pH because of the reason just mentioned in the above section. As compare to the pH effect on the ratios, dependencies of the ratios on temperature and pressure are small. However, an increase in temperature increases the pH condition where H_2S and HS^- are equally

dissolved, resulting in that pH dependencies of the ratios appear at high pH at high temperatures.

A concentration ratio of the total dissolved sulfur and chlorine is also effective parameter controlling the concentration ratio, R, since they dissolve mainly as thio and chloride complexes. As can be seen in Figure 5.5, the latter ratio, R is high when the former ratio (∑S/∑Cl) is high at medium to low pH conditions where $Au(HS)_2^-$ and $AgCl_2^-$ are predominant. On the other hand, the latter does not vary significantly with the former at high pH conditions where gold and silver dissolved as $Au(HS)_2^-$ and $Ag(HS)_2^-$, respectively.

5.3.3 Ag-Au-S minerals

Argentite has often been reported as an associated mineral with the Au-Ag solid solutions. The empirical equation to estimate fS_2 for the argentite – electrum assemblage was proposed by Barton and Toulmin (1964) as:

$$\log fS_2 = 1 / (4.576\ T) * (-41980 + 16.52\ T - 18.296\ T * \log(1-X_{Au})$$

$$+ 4 * X_{Au}\text{^}2 * (5650 - 1600 * X_{Au} - 1.375\ T).$$

where T in K. The equation was solved simultaneously with equilibria for all dissolved sulfur species to obtain fO_2.

The stability fields of argentite are plotted in Figure 5.2c and d where the compositions of the coexisting Au-Ag solid solutions (X_{Au}) are 0.4 and 0.001, respectively. However, the fields coexisting with the solid solutions of X_{Au} = 0.9 and 0.999 are restricted in very narrow fields at extremely low pH (<1).

Petrovskaite and uytenbogaardtite also possibly appear below 300°C (Pal'yanova et al., 2011) and below 183°C (Tagirov et al., 2006), respectively, with the Au-Ag solid solutions. The relations between fS_2 and T for the assemblages argentite/acanthite with the solid solution of X_{Au} = 0, uytenbogaardtite with X_{Au} = 0.25 and petrovskaite with X_{Au} = 0.5 are depicted in Figure 5.6a with the pyrite - pyrrhotite buffer and sulfur condensation lines. According to my assumption of the ideal mixing of the solid solutions, the assemblages argentite/acanthite - uytenbogaardtite and uytenbogaardtite - petrovskaite may coexist with the solid solutions of the compositional range in $0 < X_{Au} < 0.25$ and $0.25 < X_{Au} < 0.5$, respectively (Gurevich et al., 2011). Representative assemblages of argentite/acanthite - uytenbogaardtite - $Au_{1/6}Ag_{5/6}$ and uytenbogaardtite - petrovskaite - $Au_{1/3}Ag_{2/3}$ are plotted in Figure 5. 6b.

The above all assemblages appear in the pyrite stable field, so they may be able to be drown also in Figure 5.2 as the same manner as argentite - Au-Ag solid solutions in the figures, although they are not depicted in the figures to avoid complication. The mineral Au_2S is unstable in the all conditions in Figure 5.6 (Gurevich et al., 2011). Therefore I did not take it into my calculations.

5. 4 Applications

5.4.1 Ladolam geothermal system

Ladolam geothermal system is a well known active hydrothermal system

hosting one of world's largest (~1300 tons of gold, Simmons and Brown, 2006) and youngest (690 ± 26 Ka Re-Os ages of ore mineralization, Mclnnes et al., 1999) gold deposit on Lihir Island, Papua New Guinea. Simmons and Brown (2006) reported the results of in situ analyses on Ladolam geothermal fluids (Table 5.4). Although there may be no datum for gold fineness of the Au-Ag solid solution in the analyzed wells, Muller et al. (2002) suggested that Au and Ag are exited as sub-microscopic inclusions with the ratio of 0.199 (by weight) in pyrite from a drill core close to the well. Therefore, I apply my analytical procedure to the above geothermal fluids to investigate a possibility of gold mineralization with pyrite from the fluids in the well.

The temperatures and pressures of the geothermal fluids of GW06, GW14 and PW24 are tentatively assumed based on the data in Table 3 as 300°C and 15 MPa, 200°C and 5.5 MPa and 100°C and 3.6 MPa, respectively. Figures 5.7a, 5.7b and 5.7c show the analytical results of total concentrations of dissolved gold and silver in the fluids equilibrated with the Au-Ag solid solution of X_{Au} = 0.73 (gold fineness = 832) for GW06, GW14 and PW24, respectively. The all results indicate that the total concentrations of gold and silver in the pyrite fields are higher than the measured concentrations of the geothermal fluids by several orders of magnitude, that is, the measured fluids are extremely undersaturated with the Au-Ag solid solution of X_{Au} = 0.73. Hence, the fluid(s) from which the above mentioned sub-microscopic inclusions of the solid solutions precipitated with pyrite should be of the different physical conditions and/or concentrations from the current fluids in the well.

5.4.2 Woxi deposit

Since concentrations of dissolved sulfur in fluid inclusions from the Woxi deposit could not be determined, a dependency of gold finenesses on the concentration ratio of dissolved chlorine and sulfur can not be discussed.

Concentration ratios of dissolved gold and silver in the fluids equilibrated with the solid solutions of X_{Au} = 0.999 (Table 4.1) have been calculated in the pH-fO_2 conditions where pyrite is stable. Three homogenization temperatures of the inclusions in scheelite, 356°C, 303°C and 198°C (Table 4.3), and two total concentrations of dissolved sulfur species, 0.01 mol/kg and 0.1 mol/kg, have been taken into account in the calculations. Pressure corrections on homogenization temperatures have not considered in the present calculations. Figures 5.9a, b and c show the calculation results for the temperatures, 356°C, 303°C and 198°C, respectively. Stable fields of sericite (muscovite) are also depicted in the figures because it often occurs in the Woxi deposit as the hydrothermal alteration product.

The results indicate that the ratios of measured concentrations of dissolved gold and silver, R =log (∑Au/∑Ag in mole), 0.22 and 0.30 of the fluids at the temperatures, 356°C and 303°C, respectively are depicted in the fields where pyrite and sericite are stable, while the line R = 0.08 for the lowest temperature, 198°C falls into the very low pH field where sericite is unstable.

5. 5 Summary and discussion

It can be summarized from the analyses that the Au-Ag solid solutions with

high gold finenesses could precipitate from the fluids of (1) high ratios of the total concentrations of dissolved gold and silver, (2) low pH's, (3) high ratios of the total dissolved chlorine and sulfur and (4) high temperatures. The native gold in the Woxi deposit might be precipitated in the fluids of (1) and/or (4).

Although the ratios of total dissolved gold and silver in natural fluids are low as, for example, 0.004 - 0.031 in seawaters (e. g., Shikazono and Shimizu, 1987), 0.007 - 0.11 in active geothermal fluids (e. g., Henley et al., 1984; Simmons and Brown, 2007; Rae et al., 2011) and 0.0002 - 0.1 in fluid inclusions (e. g., Ulrich et al., 1999), the solid solutions of high gold finenesses may precipitate when the fluid conditions are of (2) – (4) in the above.

It can be seen in Figure 5.8 that ore-forming conditions of the deposits with higher gold finenesses are high temperatures (>350°C) and/or low pH conditions and/or high total dissolved chlorine concentrations. It may also be said that high gold finenesses have been reported from the deposits of archean, porphyry and epithermal types commonly characterized by high temperatures, high total dissolved chlorine concentrations and low pH conditions, respectively.

A precipitations mechanism of the Au-Ag solid solutions is beyond my scope. However, the following might be a possible course for increasing gold finenesses during fluid ascending. As can be seen in Figure 5.2, a favorite condition for a high gold concentration is at around the point where H_2S, HS^- and SO_4^{2-} are equally dissolved. For simplicity, let us assume that gold and silver bearing fluids ascend with slightly increasing O_2 at a constant

temperature with a condition around or below the line where H_2S and SO_4^{2-} are predominant. An increase in O_2 changes the major sulfur species from H_2S to SO_4^{2-}, resulting in shifting pH lower along the line. Then, the total silver concentration equilibrated with the solid solutions decreases largely, while that of the total gold does not. This means that the pH for their fixed ratio R in Figure 5.3 shift toward lower pH, resulting in changing the fluid condition for high gold finenesses.

Table 5.1. Gold finenesses of the Au-Ag solid solutions from 47 Au-Ag deposits with average gold and silver grades, associated minerals, gangue and alteration minerals, homogenization temperatures and salinities in fluid inclusions and types of deposits (Liang and Hoshino, 2015).

No.	Deposit	Gold fineness	Au (g/t)	Ag (g/t)	Associated minerals	Gangue & alteration minerals	H.T (℃)	Salinity (wt% NaCl equv.)	Type
1	Hemlo	709-999	8	1.5	Py,Ky,Rar,Orp,Cb,Sb	Kf-Ser-Bt-Phl-Chl-Ba	200-400	5.2-37	Archean
2	Chalice	751-971	4.9	-	Mt,Po,Mo,Qz,Di,Py,Cp	Plg–Kf-Ab-Bt-Di-Acl-Qz	465-555*	-	Archean
3	Mt. Shea	760-970	0.3	0.2	Py,Mt,Cp,Qz	Ep-Acl-Ab-Mt-Qz,Bt-Ser-Cal	300-350	2-9	Archean
4	Homestake	788-938	6.7	47	Po,Apy,Py,Qz	Qz-Cal-Bt-Ank-Sd-Chl	170-480	<10	Archean
5	Hadamengou	<800 - 919	3-8	-	Py,Qz	Kf-Qz-Mt	200-450	< 5	Archean
6	Mt Charlotte	834–857	23	172	Hes,Pz,Py,Po	Ser+Ank+Qz+Ab, Py-Ms-Po	239-310	< 6	Archean
7	Golden mile	898-972	7	3.4	Col,Cav,Pz,Kr	Acl-Ab-Ep,Cal-Chl,Py-Ms	250-350	< 5.5	Archean
8	A1 at Woods Point	941	5.50	-	Qz,Cp,Tet,Sp,Gn,Bo	Ser-Ank-Ab-Cal-Qz	155-335	1-9	Slate
9	Charters Towers	667–870	7.7	5.1	Qz,Py,Cp,Gn,Sp,Ser,Cal	Ser-Ank-Qz	240-300	5-11, 19-28	Plutonic
10	Butte	550-740	0.042	8.6	Qz,Py,Sp,Gn,Mt,Mo	Ser-Kf-Qz	370-700	2.7-4.1, 38	Porphyry
11	Bajo de la Alumbrera	600-950	0.64	2.5	Cp, minor Bn	Qz-Mt,Bt-Kf,Ab-Ser	240-787	2.7-69.7	Porphyry
12	Mineral Park	703	0.032	2.2	Qz,Py,Mt,Cp,Mo	Ser-Kf-Qz	360-450	1-13, 20-25	Porphyry
13	Bingham	850-900	0.38	3.3	Bn,Cp,Py,Act	Kf-Bt-Ser,Qz-Mo	315-500	4.3-50.8	Porphyry
14	Far Southeast	873-976	1.3	0.93	Bn,Py,Cp,Tn,Pz,Cp,Mo	Qz-Mt-Chl-Bt,Ilt-Ht	390->500	hypersaline	Porphyry

Table 5.1. (continued)

No.	Deposit	Gold fineness	Au (g/t)	Ag (g/t)	Associated minerals	Gangue & alteration minerals	H.T (℃)	Salinity (wt% NaCl equv.)	Type
15	Santo Tomas II	900-972	0.7	1.5	Cp,Bn	Mt-Ht-Qz-Bt-Anh	>500	hypersaline	Porphyry
16	Dizon	924	0.93	2	Py,Cp,Qz,Mc	Chl-Ser-Qz	270->500	hypersaline	Porphyry
19	Chaoshan	256-972	18.4	-	Po,Cp,Py,Apy	Grt-Ep-Acl-Plg,Kf-Bt-Py-Qz-Cal	255-335	17.5-37.5	Skarn
20	Big Gossan	540-960	1	16.4	Qz,Py,Po,Gn,Cp,Sp,Apy	Px-Cal-Grt,Mt-Cal-Anh-Phl-Qz	250-535	7.1, 38-65	Skarn
21	Wanagon	772-989	0.95	-	Cp,Gn,Sp,Apy,Py,Tet	Ka-Sm,Kf-Cal-Qz	160-410	<13,19-29	Skarn
22	South Hercule	427-965	2.7	147	Py,Sp,Ga,Tet	Cal,Sph-Ga-Py,Py-Ba-Qz	129-299	0.5-19.8	VMS
23	Que River	550-800	3.5	204	Py,Gn,Sp,Cp,Apy	Ms-Kf-Cal-Qz	160-250	-	VMS
24	Rosebery	560-585	2.9	155	Py,Gn,Sp,Tt,Ba	Mt-Bt,Ba-Ser,Py-Po-Qz	>330	10-25	VMS
25	Nurukawa	600-800	29.7	1288	Qz, Py,Gn,Sp,Cp,Ba	Ser-Ka-Qz	105-305	3.2-7.0	VMS
26	Shakanai	660-880	0.3	44	Py,Cp,Gn,Sp	Ms-Anh-Qz	100-240	-	VMS
27	Porgera	500-891	3.7	11.3	Py,Fb,Cp,Tet,Sp,Apy,Act	Qz-Ilt-Kf-Cal,Rsc-Cal-Anh-Dol	100-518	3-58.4	Epithermal
28	Ryuo	536-623	-	-	Gn,Cp,Act,Py,Sp	Sm/Ilt-Kf-Qz	206-238	0.35	Epithermal
29	Racetrack	540-875	31	240	Gn,Tt,Qz,Fb,Py,Cp,Apy	Ser-Pa-Ank-Ab-Ca-Qz	150-230	1-8.	Epithermal
30	Chelopech	659-983	11.6	4.1	Qz,Py,Cp,Ten,Bn,Sp,Gn	Aln-Ka-Ser-Adl-Qz	175-221	6.3-20.4	Epithermal
31	Hishikari	667-814	70.5	49	Cal,Adl,Qz,Trc,Act	Adl-Cal-Qz-Chl-Ser	175-215	0.2-2.1	Epithermal
32	Axi	701-866	5.81	10.4	Qz,Py,Mc,Asp,Ht,Lim	Qz-Cal-Adl-Qz	106-335	0.5-6.9	Epithermal

Table 5.1. (continued)

No.	Deposit	Gold fineness	Au (g/t)	Ag (g/t)	Associated minerals	Gangue & alteration minerals	H.T (℃)	Salinity (wt% NaCl equv.)	Type
33	Bilimoia	809-922	<0.2 – 1650	<0.2 – 80	Bmt,Cp,Hes,Wlf,Py,Cv,Bn, Ttd,Cav	Qz-Ilt-Ka-Ba	210-330	0.9-5.4	Epithermal
34	Bulawan	942	2.42	~2.42	Cp,Gn,Hes,Alt,Cal,Sp	Ser-Qz-Cal	153-390	0.1-6.6	Epithermal
35	Ladolam	832	5	2	Py	Bt-Mt-Kf,Qz-Ilt-Adl-Py	111-368	2.5-19.3	Epithermal
36	Conical seamount	690-893	25	216	Sp,Gn,Py,Cp	Ilt-Sm-Kf-Qz	< 310	-	Submarine
37	Sizhuang	293-776	0.0025	0.1	Qz,Py	Ser-Kf-Qz	200-340	3-14.97	Magmatism
38	Hannan South	948-999	5.4	2	Py,Qz,Gn,Chl,Amp	Ka-Hal,Qz-Amp-Chl	385-530	-	Supergene
39	Ashanti	760-990	<16.6	-	Qz,Apy,Gt,Pz,Cav	Ka-Mica-Qz	165-220	< 5	Supergene
40	Nazareno	690-820	10	260	Uy,Act,Gt,Cv	Qz,carbonate, dacite	-	-	Supergene
41	Pongkor	700-820	20	160	Uy,Act,Pr,Agv,Str,Mck	Ilt,Mln,Ba,carbonate	-	-	Supergene
42	Ulakhan	700-800	85	1200	Ac,Uy,Agv,Prc,Gt,Cv	Qz,Malh,melanterite	-	-	Supergene
43	Morning Star	780-930	-	-	Ac,Uy,Canf,Lil	Malh,carbonate,	<113	-	Supergene
44	Broken Hills	370-620	-	-	Uy,Cv,Act,Pet,Agv,Py	Qz,Ba,Adl	-	-	Supergene

Table 5.1. (continued)

No.	Deposit	Gold fineness	Au (g/t)	Ag (g/t)	Associated minerals	Gangue & alteration minerals	H.T (℃)	Salinity (wt% NaCl equv.)	Type
45	Nilambur	921-975	1	< 10	Py,Po,Ilm,Cp	Qz-Ser-Chl	280-360	2-14.	Primary
		982-1000	1.1	1.38	Ht, La	La, weathering profiles	-	-	Supergene
		985-1000	-	-	stream grave, pebble	La matrix	-	-	Placer
46	VCR at Vaal Reefs	832-943	5-12	-	Qz,Po,Chl,Gn	Qz-Cal,Prl-Ms-Chl	133-208	2.3-6.6	Placer
47	Free State Geduld	906-935	35.2	3.3	Py,Qz,Urn,Tcl,Gn	Qz-Cal-Chl	127-142	1.5-12	Placer

H.T is homogenization temperature determined in fluid inclusions; * is peak-metamorphic temperatures.

Abbreviation of minerals: Ab (albite); Acl (actinolite); Act (acanthite); Adl (adularia); Agv (aguilarite); Aln (alunite); Alt (altaite); Amp (amphibole); Anh (anhydrite); Ank (ankerite); Apy (arsenopyrite)Agt; Ba (barite); Bmt (bismuthinite); Bo (Bournonite); Bt (Biotite); Cal (calcite); Canf (canfieldite); Cav (calaverite); Cb (cinnabar); Col (coloradoite); Cp (chalcopyrite); Cv (Covellite); Di (diopside); Dol (dolomite); Ep (epidote); Fb (freibergite); Fo (forsterite); Gn (galena); Grt (garnet); Gt (goethite); Hal (halloysite); Hbl (hornblende); Hes (hessite); Ht (hematite); Ilm (ilmenite); Ilt (illite); Ka (Kaolinite); Kf (K-feldspar); Kr (krennerite); Ky (kyanite); La (laterite); Lil (lillianite); Lim (limonite); Malh (malachite); Mc (marcasite); Mck (mckinstryite); Mln (montmorillonite); Ms (muscovite); Mt (magnetite); Op (orpiment); Pa (paragonite); Pet (petrovskaite); Phl (phlogopite); Plg (plagioclase); Po (pyrrhotine); Prl (pyrophyllite); Pr (proustite); Px (pyroxene); Py (pyrite); Pz (petzite); Qz (quartz); Rar (realgar); Rsc (Roscoelite); Sd (siderite); Ser (sericite); Sm (smectite); Sp (sphalerite); Str(stromeyerite); Tcl (thucholite); Tet (tetrahedrite); Tn (tennantite); Trc (truscottite); Ttd (tetradymite); Ttn (titanite); Urn (uraninite); Uy (uytenbogaardtite); Wlf (wolframite);

References with number of deposits: 1 Cameron and Hattori, 1985; Harris, 1986; Pan and Fleet, 1995; Muir, 2002; 2 Bucci et al., 2002; 3 Mueller, 2007; 4 Desborough et al., 1971; Caddey et al., 1991; Uzunlar et al, 2010; 5 Gan et al., 1994; 6 Mueller and Muhling, 2013; Bateman and Hagemann, 2004; Rasmussen et al., 2009; Mernagh et al., 2004; 7 Mueller and Muhling, 2013; Bateman and Hagemann, 2004; 8 Green et al., 1982; 9 Kreuzer, 2006 and

Kreuzer et al., 2007; NRM, 2012; 10 Rusk et al., 2004 and 2008; Antweiler and Campbell, 1977; Singer et al., 2005; 11 Chryssoulis, 2001; Murakami et al., 2010; Ulrich et al., 2002; 12 Lang and Eastoe, 1988; Antweiler and Campbell, 1977; Singer et al., 2005; 13 Landtwing et al., 2010; Seo et al., 2009; Morrison et al., 1991; Fisher, 1945; 14 Akira, 2000; Singer et al., 2005; 15 Akira, 2001; Singer et al., 2005; 16 Akira, 2005; Singer et al., 2005; 17 Rubin and Kyle, 1997; Lu, 2000; Ulrich et al., 1999; 18 Prendergast et al., 2005; Rubin and Kyle,1997; 19 Wang et al., 2008; Hu et al., 2001; Yang et al., 2008; 20 Meinert et al., 1997; Prendergast et al., 2005; Rubin and Kyle,1997; 21 Meinert et al., 1997; Prendergast et al., 2005; 22 Zaw and Large, 1992; 23 Huston and Large, 1989; Morrison et al., 1991; 24 Huston and Large, 1989; Zaw et al., 1999; Zaw and Large, 1996; 25 Huston and Large, 1989; Yamada et al., 1987; Sasaki et al., 1995; 26 Kajiwara, 1971; Sato, 1974; Tanimura et al., 1983; 27 O'Dea, 1980; Richards, 1990; Richards et al.,1991; 28 Maeda,1998; 29 Mariam et al., 1993; 30 Bonev et al., 2002; Moritz, 2006; 31 Izawa et al., 1990; Etoh et al., 2002; Akira et al., 1998; Akira and Tadakazu, 2002; 32 Zhai et al., 2009; 33 Espi et al., 2007; 34 Maglambayan et al., 1998; 35 Muller et al., 2002; 36 Petersen et al., 2002; 37 Qian et al., 2011; 38 Lawrance and Griffin, 1994; Mueller et al., 2012; 39 Bowell, 1992; Bowell et al., 1990; 40 Greffie et al., 2002; Pal'yanova and Savva, 2008; 41 Greffie et al., 2002; Pal'yanova and Savva, 2008; 42 Pal'yanova and Savva, 2008;43 Sheets et al., 1995; Pal'yanova and Savva, 2008; 44 Cocker et al. 2013; 45 Nair et al., 1987; Santosh et al., 1992; Binu-Lal et al., 2003; 46 Frimmel and Gartz,1997; Reid et al., 1988; 47 Saager, 1969; Frimmel et al., 1999.

Table 5.2. Aqueous species of gold and silver and their formation reactions counted in the present analyses (Liang and Hoshino, 2015).

Species	Reactions
Au^+	$Au(s) + H^+ + 1/4O_{2(aq)} = Au^+ + 1/2H_2O$
$AuOH_{(aq)}$	$AuOH_{(aq)} + H^+ = Au^+ + H_2O$
$AuCl_{(aq)}$	$AuCl_{(aq)} = Au^+ + Cl^-$
$AuCl_2^-$	$AuCl_2^- = Au^+ + 2Cl^-$
$AuCl_3^-$	$AuCl_3^- = Au^+ + 3Cl^-$
$AuHS_{(aq)}$	$AuHS_{(aq)} = Au^+ + HS^-$
$Au(HS)_2^-$	$Au(HS)_2^- = Au^+ + 2HS^-$
Ag^+	$Ag(s) + H^+ + 1/4O_{2(aq)} = Ag^+ + 1/2H_2O$
$AgOH_{(aq)}$	$AgOH_{(aq)} + H^+ = Au^+ + H_2O$
$Ag(OH)_2^-$	$Ag(OH)_2^- + 2H^+ = Au^+ + 2H_2O$
$AgCl_{(aq)}$	$AgCl_{(aq)} = Ag^+ + Cl^-$
$AgCl_2^-$	$AgCl_2^- = Ag^+ + 2Cl^-$
$AgCl_3^-$	$AgCl_3^- = Ag^+ + 3Cl^-$
$AgCl_4^-$	$AgCl_4^- = Ag^+ + 4Cl^-$
$AgHS_{(aq)}$	$AgHS_{(aq)} = Ag^+ + HS^-$
$Ag(HS)_2^-$	$Ag(HS)_2^- = Ag^+ + 2HS^-$

Table 5.3. Thermodynamic functions, parameters of the Maier-Kelley equation for heat capacities and molar volumes of petrovskaite (P) and uytenbogaardtite (U) taken into the SUPCRT92 data set (see text) (Liang and Hoshino, 2015). Temperature limits for petrovskaite and uytenbogaardtite are 583 K and 456 K, respectively.

	$\triangle G_f^0$ cal/mol	$\triangle H_f^0$ cal/mol	S^0 cal/mol	a(10^0) cal mol^{-1} K^{-1}	b(10^3) cal mol^{-1} K^{-2}	c(10^{-5}) cal mol^{-1} K	V_m cm^3/mol
P	-6596.6	-5927.3	31.453	18.27	0.263	-0.949	35.463
U	-16584.6	-14149.1	65.344	36.56	0	0	69.607

Table 5.4. In situ analyses of the geothermal fluids in the Ladolam geothermal systems (data taken from Simmons and Brown, 2006).

Geothermal fluids	Au (µg/kg)	Ag (µg/kg)	pH (lab)	T (°C)	Cl^- (mol/kg)	ΣS (mol/kg)	Depth (m)
GW06	16	6	8.58	>250	0.56	0.33	1500
GW14	13	5	8.69	<260	0.55	0.31	550
PW24	1	<1	6.76	<110	0.19	0.08	360

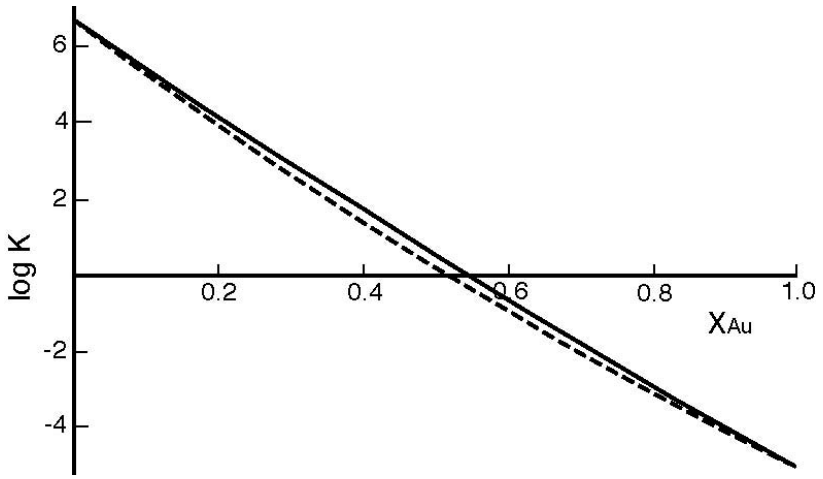

Figure 5.1. The difference in log K of the dissolution reaction of Au_XAg_{1-X} calculated by the ideal solid solution model (solid line) and by the mixing model of White et al. (1957) (broken line) (Liang and Hoshino, 2015).

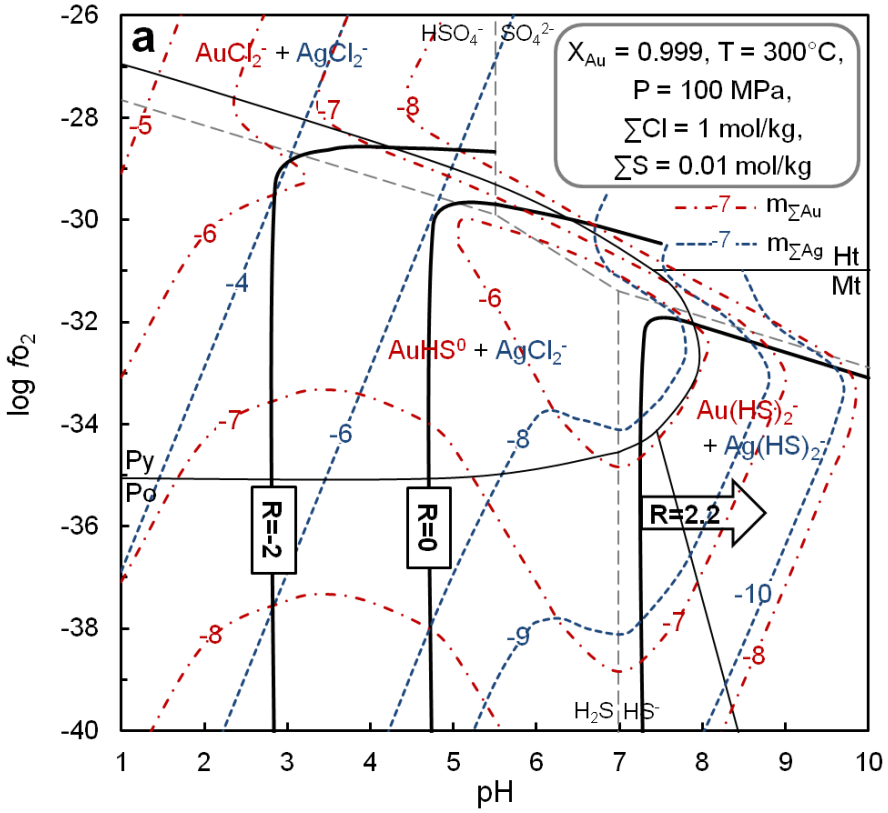
a
$AuCl_2^-$ + $AgCl_2^-$
HSO_4^-
SO_4^{2-}
X_{Au} = 0.999, T = 300°C,
P = 100 MPa,
∑Cl = 1 mol/kg,
∑S = 0.01 mol/kg
$m_{\Sigma Au}$
$m_{\Sigma Ag}$
Ht
Mt
$AuHS^0$ + $AgCl_2^-$
$Au(HS)_2^-$
+ $Ag(HS)_2^-$
Py
Po
R=-2
R=0
R=2.2
H_2S HS^-
log fo_2
pH

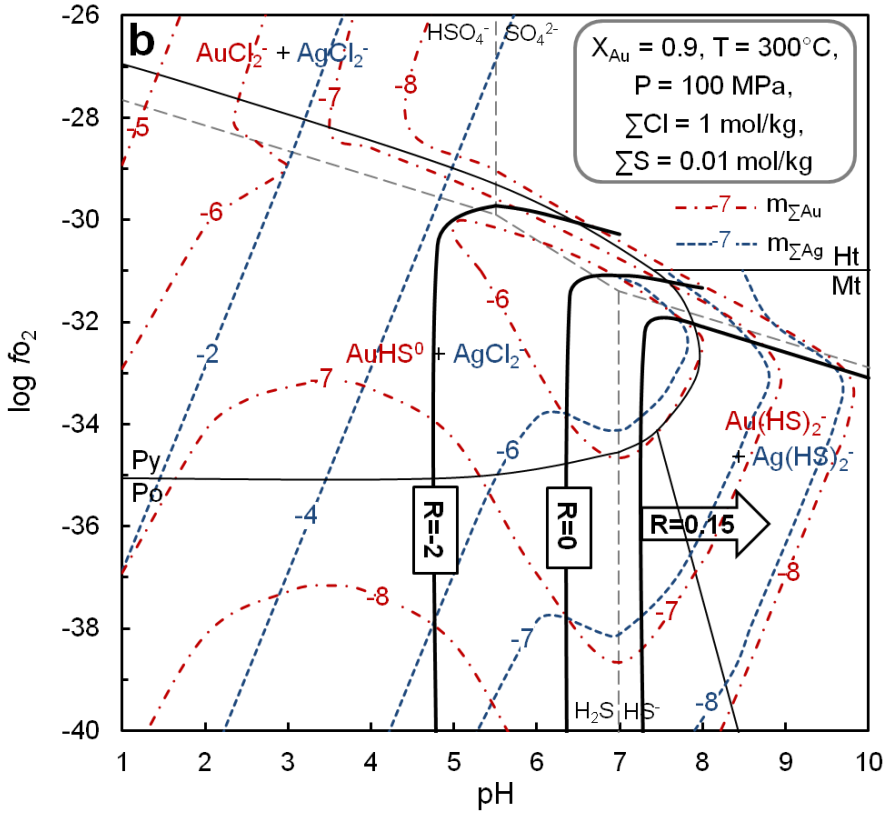
b
$AuCl_2^-$ + $AgCl_2^-$
HSO_4^-
SO_4^{2-}
X_{Au} = 0.9, T = 300°C,
P = 100 MPa,
∑Cl = 1 mol/kg,
∑S = 0.01 mol/kg
$m_{\Sigma Au}$
$m_{\Sigma Ag}$
Ht
Mt
$AuHS^0$ + $AgCl_2^-$
$Au(HS)_2^-$
+ $Ag(HS)_2^-$
Py
Po
R=-2
R=0
R=0.15
H_2S HS^-
log fo_2
pH

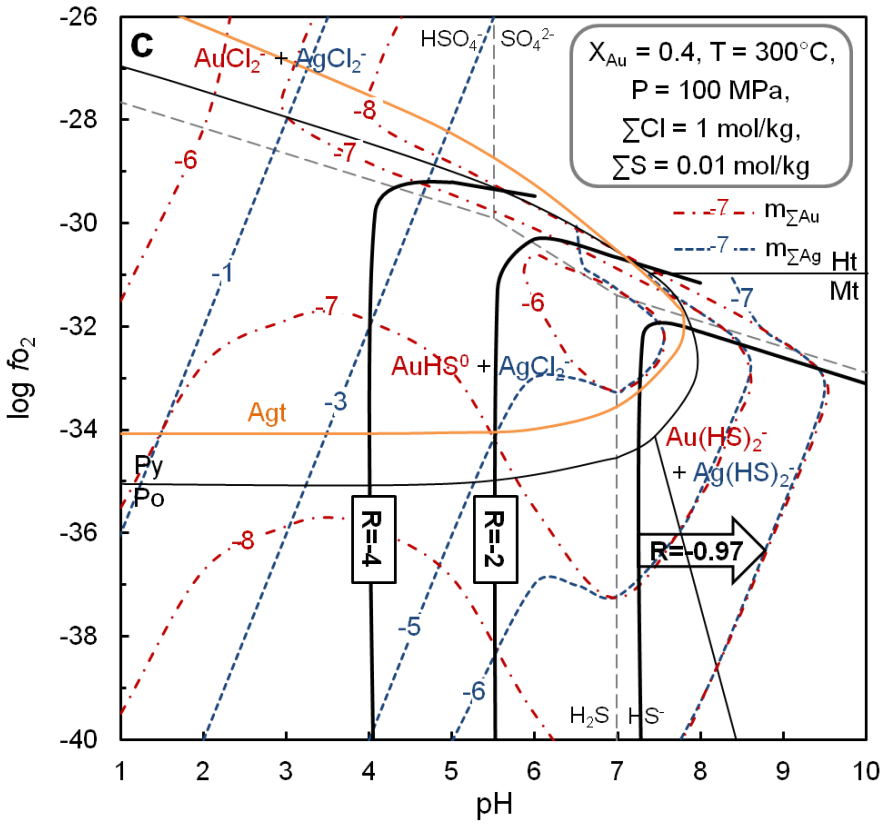
c
X_{Au} = 0.4, T = 300°C,
P = 100 MPa,
∑Cl = 1 mol/kg,
∑S = 0.01 mol/kg
$m_{\sum Au}$
$m_{\sum Ag}$
Ht
Mt
$AuCl_2^-$ + $AgCl_2^-$
HSO_4^-
SO_4^{2-}
$AuHS^0$ + $AgCl_2^-$
Agt
Py
Po
$Au(HS)_2^-$
+ $Ag(HS)_2^-$
R=4
R=2
R=-0.97
H_2S
HS^-
log fO_2
pH

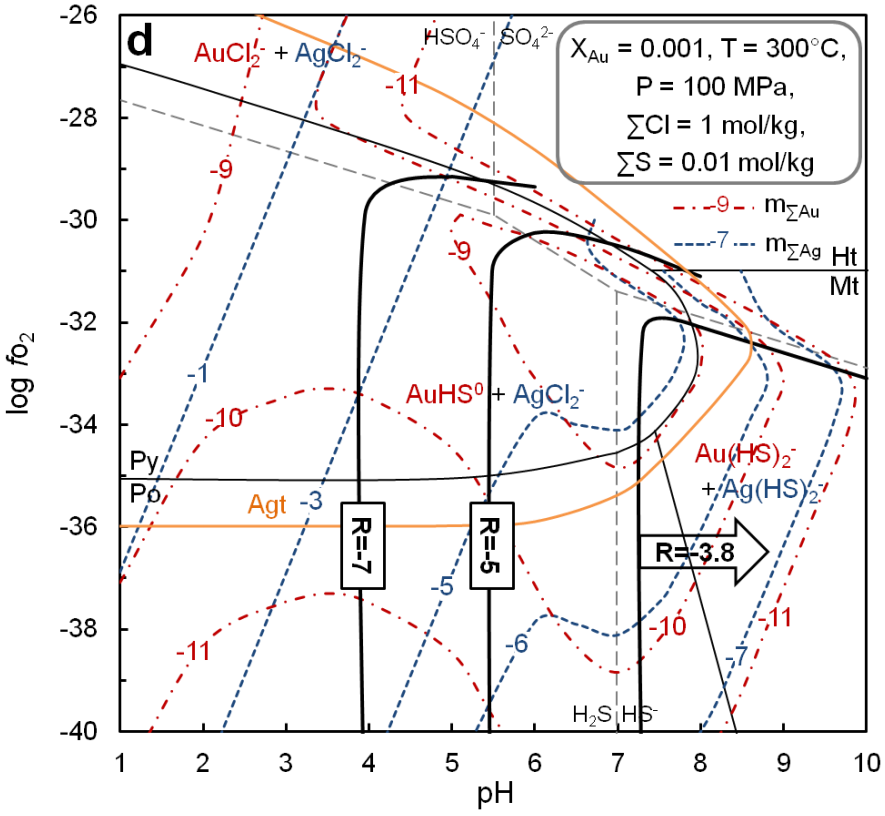
d
X_{Au} = 0.001, T = 300°C,
P = 100 MPa,
∑Cl = 1 mol/kg,
∑S = 0.01 mol/kg
$m_{\sum Au}$
$m_{\sum Ag}$
Ht
Mt
$AuCl_2^-$ + $AgCl_2^-$
HSO_4^-
SO_4^{2-}
$AuHS^0$ + $AgCl_2^-$
Agt
Py
Po
$Au(HS)_2^-$
+ $Ag(HS)_2^-$
R=7
R=5
R=-3.8
H_2S
HS^-
log fO_2
pH

Figure 5.2. logfO_2-pH diagrams showing the total concentrations of gold and silver and their ratio (R = log (∑Au/∑Ag)) of the fluids equilibrated with the Au-Ag solid solutions of the compositions, X_{Au} = 0.999 (a), 0.9 (b), 0.4 (c) and 0.001 (d) at T = 300°C and P = 100 MPa with total dissolved chlorine and sulfur as 1 mol/kg and 0.01 mol/kg, respectively (Liang and Hoshino, 2015).

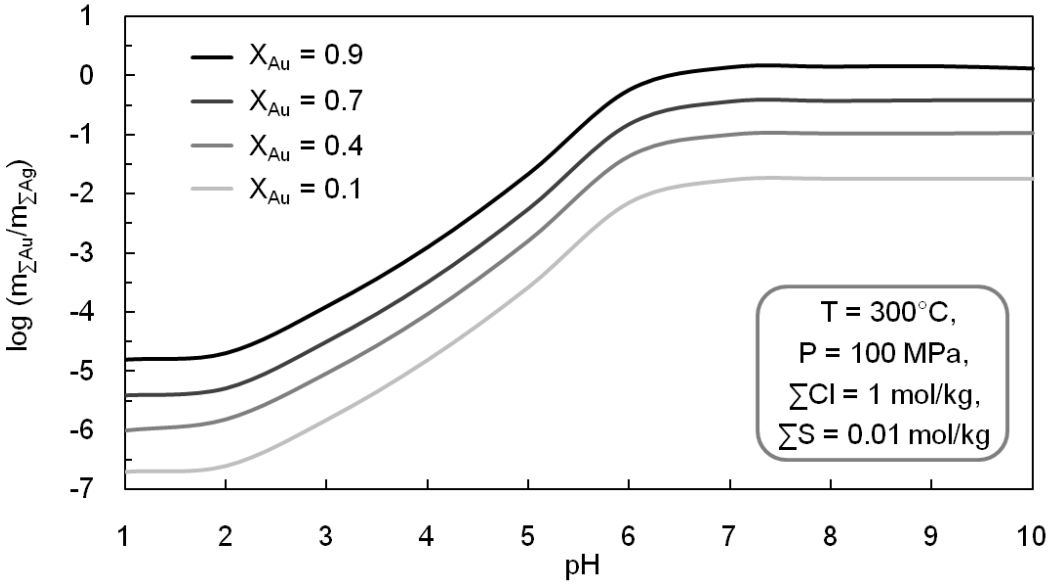

Figure 5.3. Dependencies of the ratios, Rs in the fluids equilibrated with the Au-Ag solid solutions of the compositions of X_{Au} = 0.9, 0.7, 0.4 and 0.1 on pH at the fixed fO_2 (log fO_2 = -35) (Liang and Hoshino, 2015). Other conditions are typed in the figure.

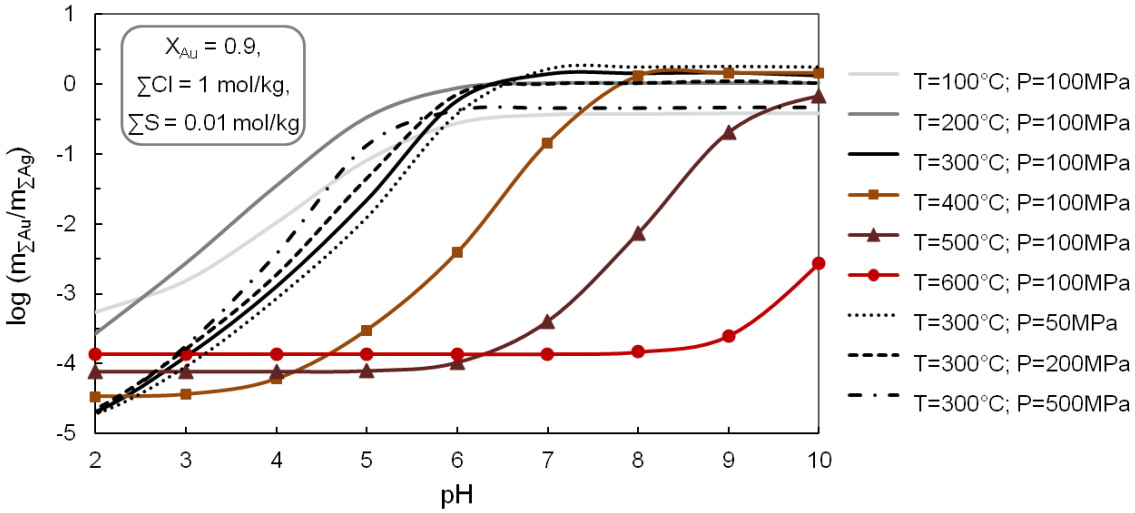

Figure 5.4. Dependencies of the ratios, Rs in the fluids equilibrated with the Au-Ag solid solutions of the compositions of X_{Au} = 0.9 on temperature and pressure at the fixed fO_2 (log fO_2 = -35) (Liang and Hoshino, 2015). Other conditions are typed in the figure.

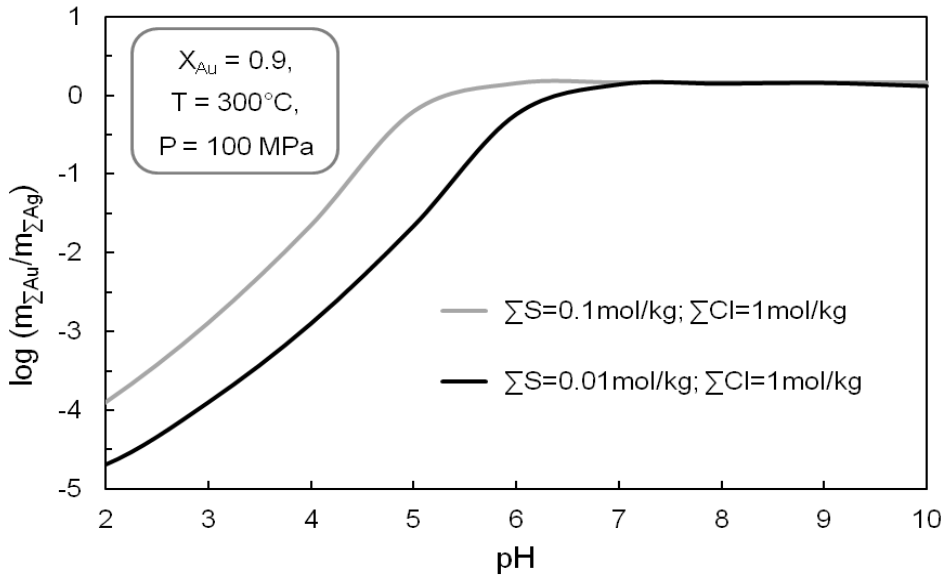

Figure 5.5. Dependencies of the ratios, Rs in the fluids equilibrated with the Au-Ag solid solutions of the compositions of X_{Au} = 0.9 on the total dissolved chlorine and sulfur at the fixed fO_2 (log fO_2 = -35) (Liang and Hoshino, 2015). Other conditions are typed in the figure.

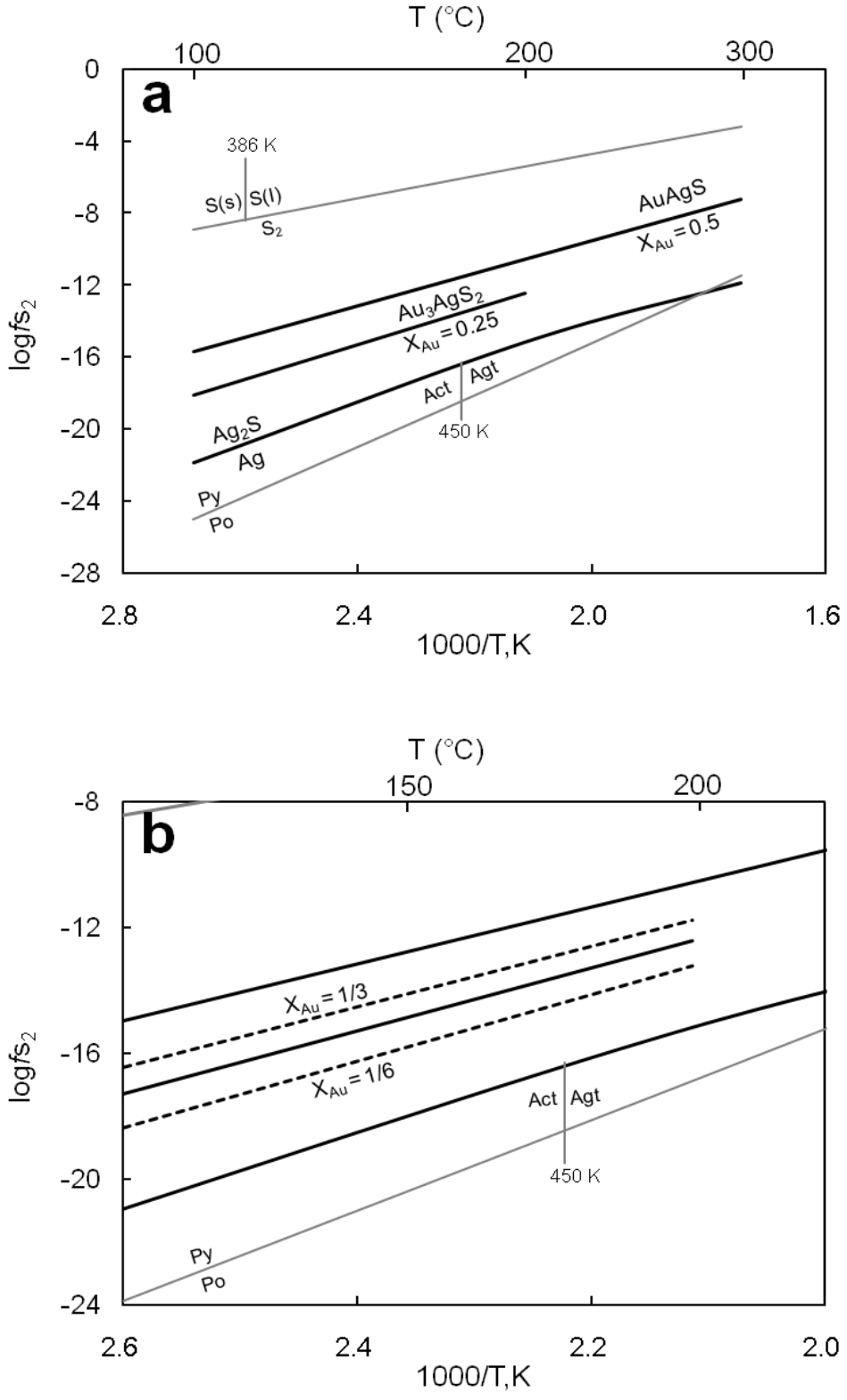

Figure 5.6. log fS_2-T diagrams showing the assemblages of Au-Ag solid solutions with argentite/acanthite, uytenbogaardtite and petrovskaite (a) and

representative compositions of the solid solutions with the assemblages argentite/acanthite - uytenbogaardtite (lower broken line) and uytenbogaardtite - petrovskaite (upper) (b) at 100 MPa (Liang and Hoshino, 2015). See text for details.

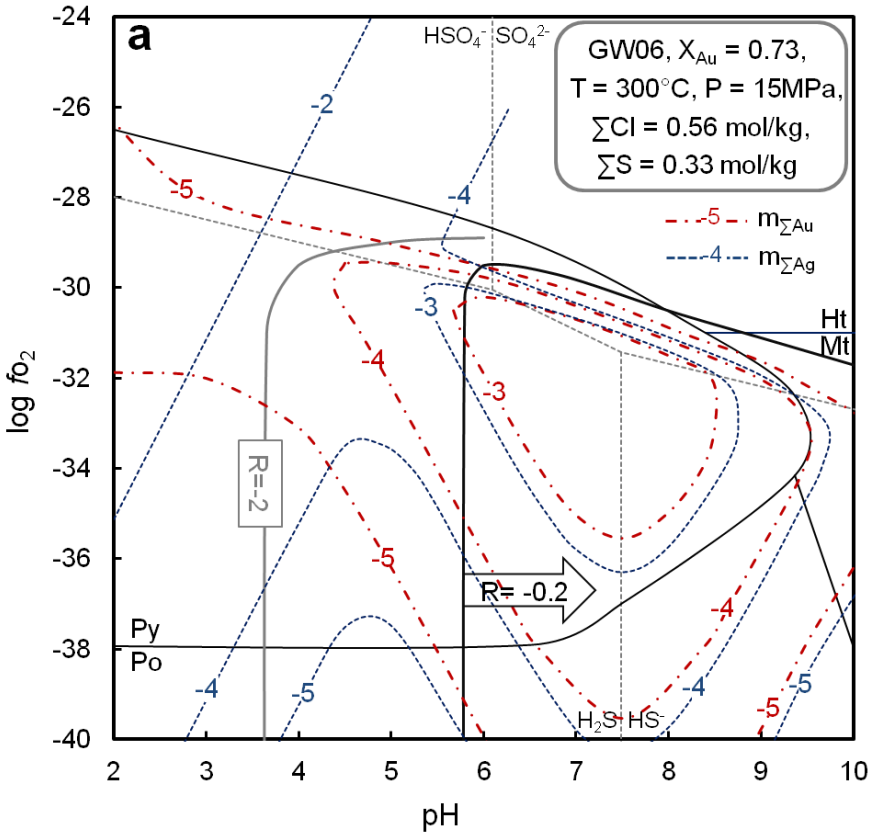
a
GW06, X_Au = 0.73,
T = 300°C, P = 15MPa,
∑Cl = 0.56 mol/kg,
∑S = 0.33 mol/kg
-5 m∑Au
-4 m∑Ag
HSO4- SO4 2-
H2S HS-
Ht
Mt
Py
Po
R=-2
R= -0.2
log fO2
pH

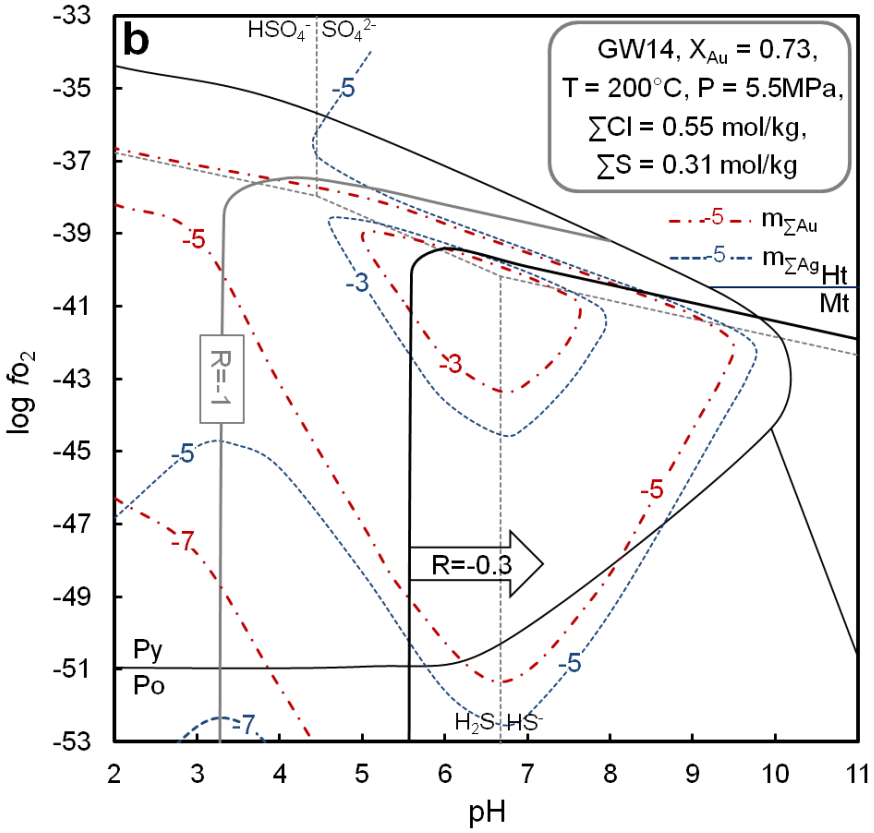
b
GW14, X_Au = 0.73,
T = 200°C, P = 5.5MPa,
∑Cl = 0.55 mol/kg,
∑S = 0.31 mol/kg
-5 m∑Au
-5 m∑Ag
HSO4- SO4 2-
H2S HS-
Ht
Mt
Py
Po
R=-1
R=-0.3
log fO2
pH

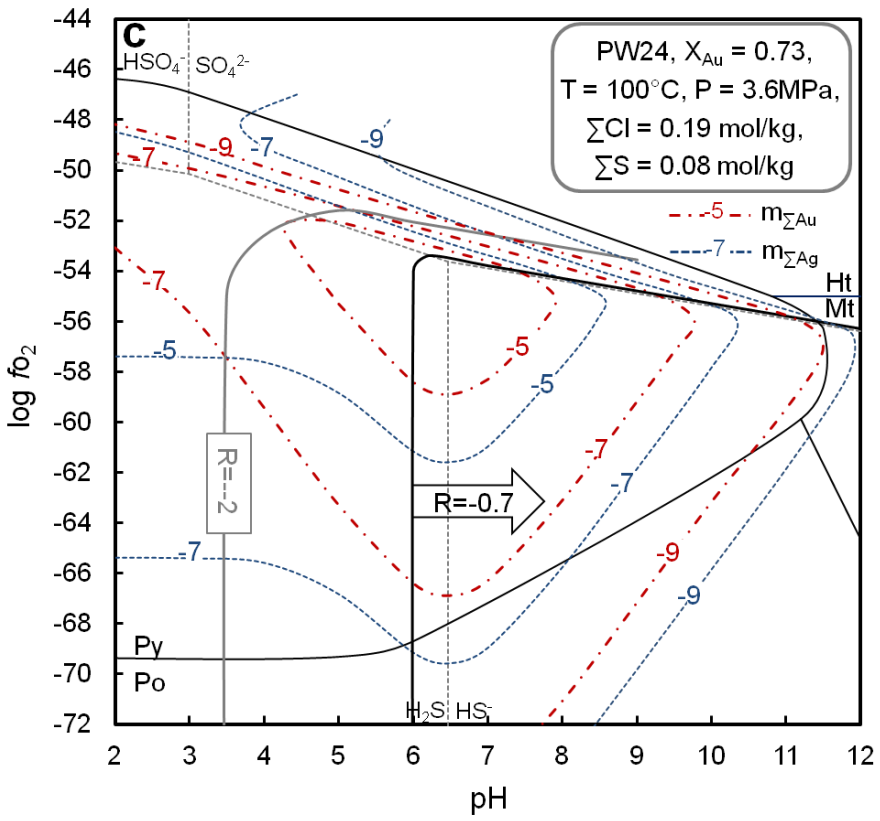

Figure 5.7. logfO_2-pH diagrams showing the total concentrations of gold and silver and their ratios, Rs of the fluids equilibrated with the Au-Ag solid solutions of the compositions X_{Au} = 0.73 for the conditions of GW06 (a), DW14 (b) and PW24 (c) (Liang and Hoshino, 2015).

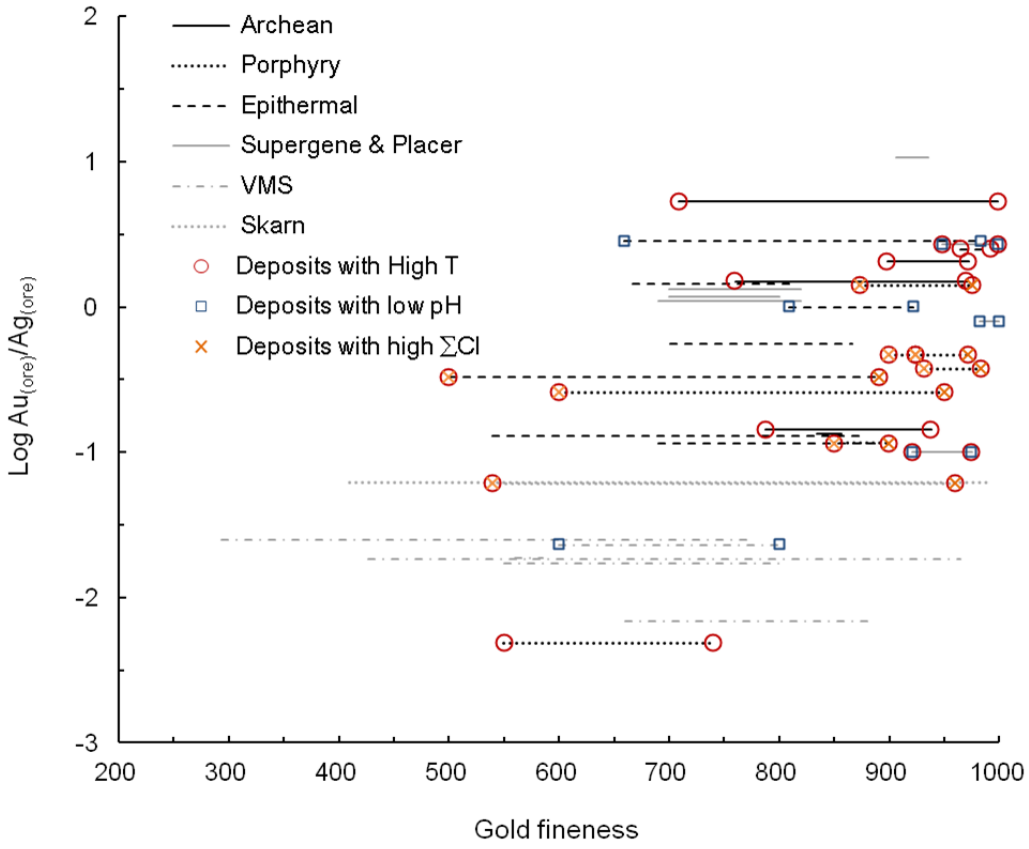

Figure 5.8. Ranges of gold finenesses and ratios of average gold and silver grades ($logm_{Au(ore)}/m_{Ag(ore)}$) in the Au-Ag deposits listed in Table 5.1 (Liang and Hoshino, 2015). Deposits including positive conditions for high gold finenesses are marked.

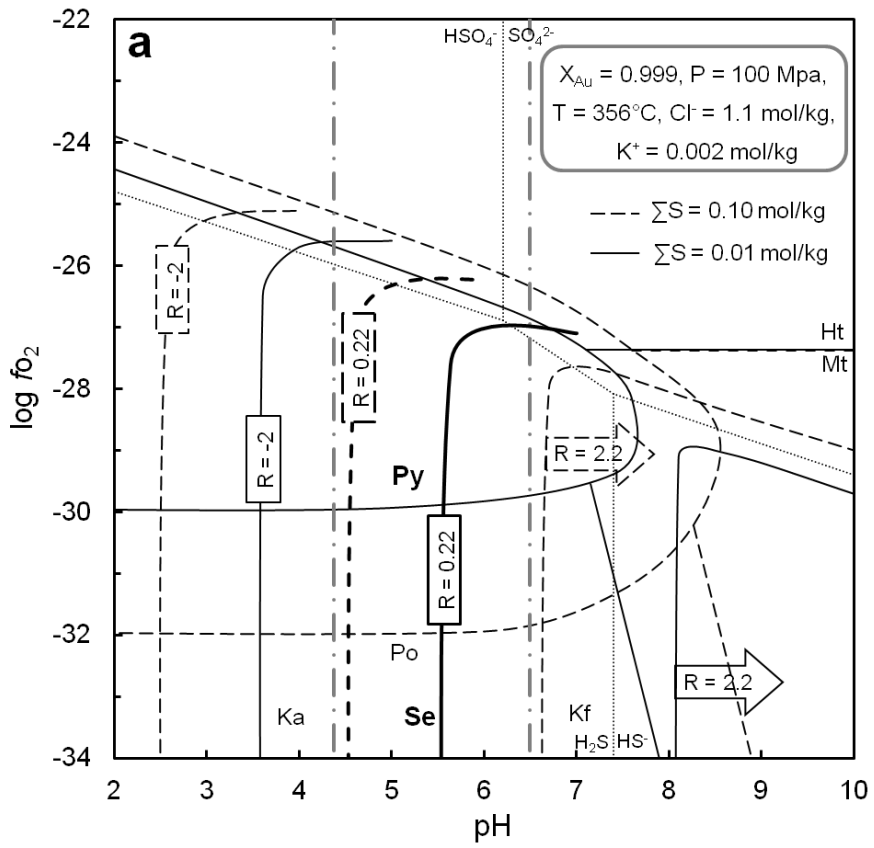
a
HSO_4^- SO_4^{2-}
X_{Au} = 0.999, P = 100 Mpa,
T = 356°C, Cl^- = 1.1 mol/kg,
K^+ = 0.002 mol/kg
∑S = 0.10 mol/kg
∑S = 0.01 mol/kg
R = -2
R = 0.22
R = -2
R = 2.2
Py
R = 0.22
Ht
Mt
Po
Ka
Se
Kf
H_2S HS^-
R = 2.2
log fO_2
pH

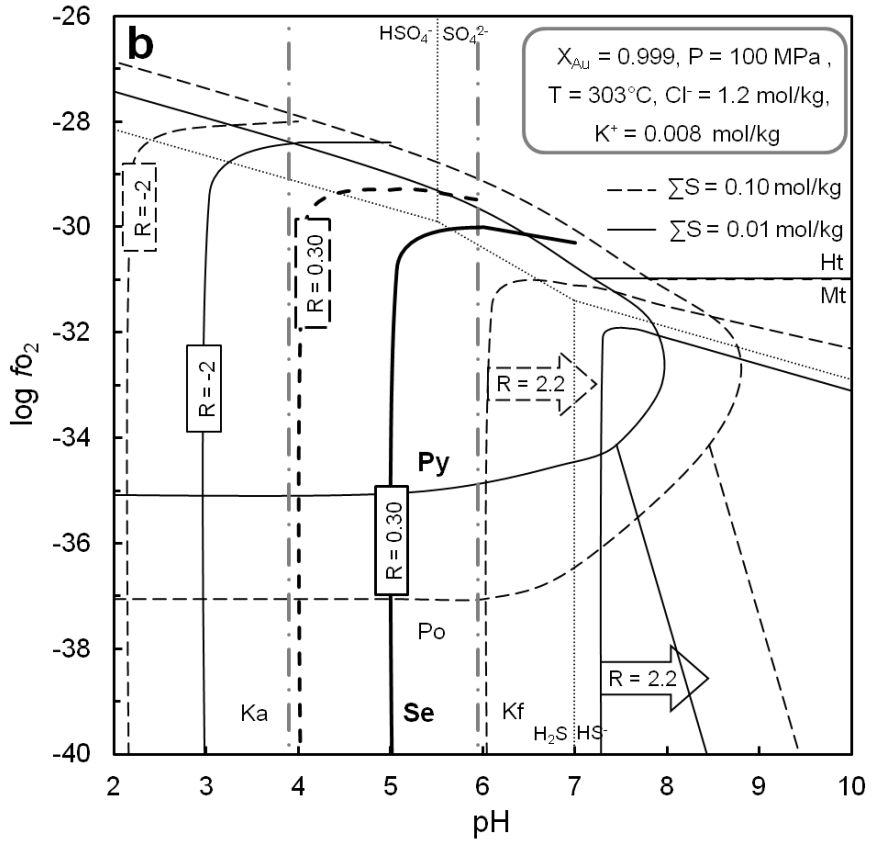
b
HSO_4^- SO_4^{2-}
X_{Au} = 0.999, P = 100 MPa ,
T = 303°C, Cl^- = 1.2 mol/kg,
K^+ = 0.008 mol/kg
∑S = 0.10 mol/kg
∑S = 0.01 mol/kg
R = -2
R = 0.30
R = -2
R = 2.2
Py
R = 0.30
Ht
Mt
Po
Ka
Se
Kf
H_2S HS^-
R = 2.2
log fO_2
pH

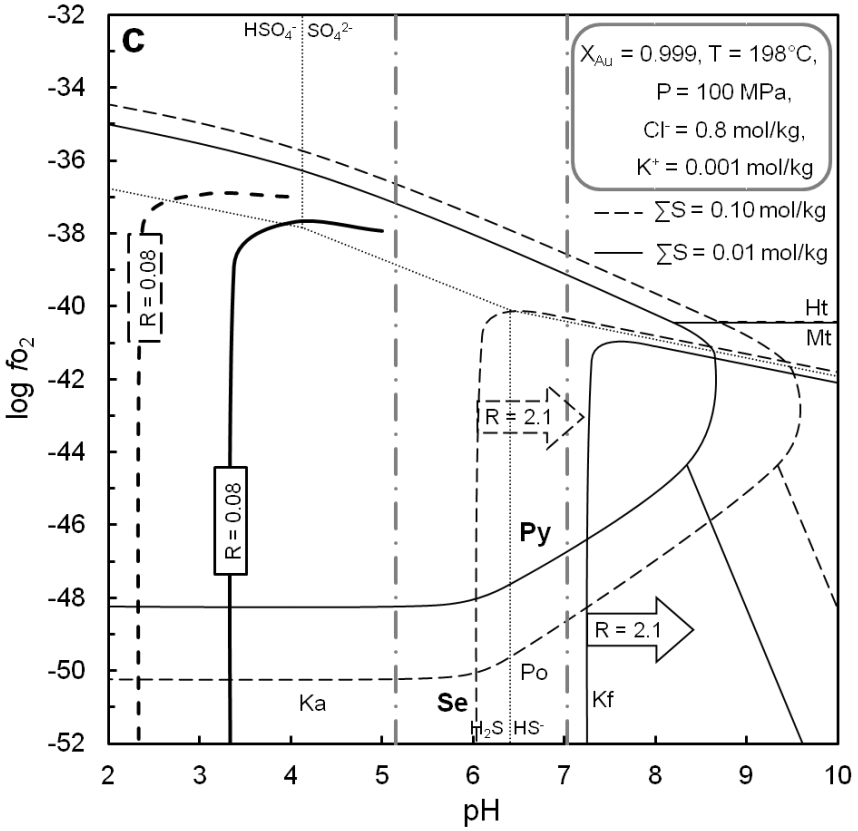

Figure 5.9. logfO_2-pH diagrams showing the ratios of total concentrations of gold and silver in fluids equilibrated with the Au-Ag solid solutions of the compositions X_{Au} = 0.999 at the temperatures, 356°C (a), 303°C (b) and 198°C (c).

6. Discussion

6.1 Native gold mineralization

Although the microscopic observations indicate the mineralogical sequence in the Woxi deposit as, from early to late, coarse-grained pyrite – scheelite – stibnite – Pb-Sb-S minerals – sphalerite (+ cubanite) – fine-grained pyrite, the mineralization stage of native gold could not be identified from the observations. However, the LA-ICP-MS analyses revealed that the high Au concentrations were detected only in the fluid inclusions in scheelite, implying the same stage of native gold mineralization with scheelite (Figure 6.1).

The EPMA analyses of native gold show their extremely high gold finenesses (Table 4.1). On the other hand, the LA-ICP-MS analyses of the fluid inclusions in scheelite have clarified the high Au/Ag ratios (Table 4.3) as compared with those in seawaters (e. g., Shikazono and Shimizu, 1987; Minoru et al., 1988), other gold deposits (e. g., Ulrich et al., 1999 and 2002; Landtwing et al., 2010) and active geothermal fluids (e. g., Koga, 1961; Brown, 1986; Henley et al., 1984; Rae et al., 2011). It is summarized from the thermodynamic calculations that the Au-Ag solid solutions with high gold finenesses could precipitate from the fluids of (1) high ratios of the total concentrations of dissolved gold and silver, (2) low pH's, (3) high ratios of the total dissolved chlorine and sulfur and (4) high temperatures. Therefore, the high gold finenesses of native gold in the Woxi deposit might have been precipitated from the fluids of high Au/Ag ratios observed in the fluid inclusions in scheelte.

6.2 Ore-forming fluids and related mineralizations

The microthermometric and LA-ICP-MS analyses of the fluid inclusions in scheelite, quartz associated with scheelite and stibnite and barren quartz clarified the characteristics of hydrothermal fluids in the Woxi deposit. Scheelite and native gold precipitated from the fluid of high temperature and salinity with high concentrations of the metal elements. Scheelite continued to precipitate followed by stibnite also from the fluid of high temperature and salinity with high concentrations of the metal elements as is observed in quartz associated with the both minerals. The later fluid of the highest temperature and salinity with low concentrations of the metal elements yielded the sphalerite mineralization. The latest fluid of low temperature and salinity with low concentrations of the metal elements is observed mainly in barren quartz and was probably trapped as secondary inclusions in the other minerals and early quartz coexisting with scheelite and stibnite.

Therefore, there might be at least three types of hydrothermal fluids during the vein formation in the Woxi deposit. Although the sources of those fluids could not be specified in the present study, the later highest temperature fluid precipitating sphalerite may imply a role of an igneous activity during the mineralization.

Mineral	Mineralization stage
Quartz	----------
Pyrite	------ ----
Scheelite	----------
Stibnite	----------
Native gold	------
Pb-Sb-S minerals	--
Sphalerite	----
Cubanite	--

Figure 6.1. The mineralogical sequence in the Woxi deposit (Liang et al., 2015).

7. Conclusion

The Woxi Au-Sb-W deposit occurs in the Madiyi Formation of the Proterozoic Banxi Group in the western Hunan Province in China. A large number of quartz veins occur mainly in the silicified slates of the Madiyi Formation in the deposit. The ore mineralization is observed mostly in the quartz veins, while rare in the host slates.

Minerals found in the deposit are mainly scheelite, stibnite, native gold, pyrite and quartz with minor amounts of sphalerite, cubanite and Pb-Sb-S minerals, zinkenite and plagionite. The mineralogical sequence identified by microscopic observations of ores is, from early to late, coarse-grained pyrite – scheelite – stibnite – Pb-Sb-S minerals – sphalerite (+ cubanite) – fine-grained pyrite. The high concentrations of Au in the fluid inclusions in scheelite detected by LA-ICP-MS analyses indicate that native gold might have precipitated with scheelite.

The microthermometric and LA-ICP-MS analyses of the fluid inclusions in scheelite, quartz associated with scheelite and stibnite and barren quartz clarified that there might be at least three types of hydrothermal fluids during the vein formation in the Woxi deposit. Scheelite and native gold precipitated from the fluid of high temperature and salinity with high concentrations of the metal elements, followed by stibnite precipitation. The later fluid of the highest temperature and salinity with low concentrations of the metal elements yielded the sphalerite mineralization. The latest fluid of low temperature and salinity with low concentrations of the metal elements is observed mainly in

barren quartz. The later highest temperature fluid precipitating sphalerite may imply a role of an igneous activity during the mineralization.

The extremely high gold finesses, 998.6 – 1000, of native gold in the Woxi deposit were probably due to the high Au/Ag ratios and high temperatures of the fluid yielding native gold mineralization with scheelite.

Acknowledgments

First and foremost, I must give my deepest thanks to my supervisor Prof. Kenishi Hoshino for his guidance during my master and doctor studies. He continually challenged and expanded my scientific boundaries, and allowed my Ph.D. experience to be an intellectual cornerstone for my future career. I would like to thank Prof. Xiangping Gu of the Central South University in Hunan Province, China for his constructive suggestions. I also would like to express my sincere thanks to the Prof. G. A. Pal'yanova for her comments and constructive suggestions to one of my published papers. I deeply acknowledge Prof. Yoshio Takahashi, since he kindly allowed me to use his LA-ICP-MS instrument. I am grateful to Mr. Yasuhiro Shibata, Mr. Yuta Yoshie and Dr. Aya Katsube for their technical supports in EPMA and LA-ICP-MS analyses. My field works in 2010 was financially supported by the Society of Resource Geology and the Japan Mining Promotive Foundation, which are gratefully acknowledged. I have to thank Japanese Government for giving me MEXT Scholarship during my doctor course. I also have to thank referees of my doctoral thesis: Prof. Naoki Suda, Prof. Toshimori Sekine, Prof. Hiroshi Hidaka, Prof. Ikuo Katayama and Prof. Kenishi Hoshino. Finally, I must thank my wife, Dan Chen, for her supports and sacrifices in the past few years.

References

Akira, I., Hidehiko, S., Tomoko, S. (1998) Hydrogen Isotope Study of Fluid Inclusions in Vein Quartz of the Hishikari Gold Deposits, Japan. Resour. Geol. 48, 159–170.

Akira, I., 2000. Mineral paragenesis, fluid inclusions and sulfur Isotope systematics of the Lepanto Far Southeast Porphyry Cu-Au Deposit, Mankayan, Philippines. Resour. Geol. 50, 151–168.

Akira, I., 2001. Generation and evolution of ore fluids for Porphyry Cu-Au mineralization of the Santo Tomas II (Philex) deposit, Philippines. Resour. Geol. 51, 71–96.

Akira, I., 2005. Evolution of hydrothermal system at the Dizon Porphyry Cu-Au deposit, Zambales, Philippines. Resour. Geol. 55, 73–90.

Akira, I., Tadakazu, U., 2002. Association of Electrum and Calcite and Its Significance to the Genesis of the Hishikari Gold Deposits, Southern Kyushu, Japan. Resour. Geol. 52, 381–394.

Antweiler, J.C., and Campbell, W.L., 1977. Application of gold compositional analyses to mineral exploration in the United States. J. Geochem. Explor. 8, 17-29.

Bateman, R., Hagemann, S., 2004. Gold mineralisation throughout about 45 Ma of Archaean orogenesis: protracted flux of gold in the Golden Mile, Yilgarn craton, Western Australia. Mineral. Deposita 39, 536-559.

Barton, P.B., Toulmin, P., 1964. The electrum-tarnish method for the determination of the fugacity of sulfur in laboratory sulfide systems. Geochim. Cosmochim. Acta 28, 619-640.

Binu-Lal, S. S., Sawaki, T., Wada, H., Santosh, M., 2003. Ore fluids associated with the Wynad gold mineralization, southern India: evidence from fluid inclusion microthermometry and gas analysis. J. Asian Earth Sci. 22, 171–187.

Bonev, I. K., Kerestedjian, T., Atanassova, R., Andrew, C. J., 2002. Morphogenesis and composition of native gold in the Chelopech volcanic-hosted Au–Cu epithermal deposit, Srednogorie zone, Bulgaria. Mineral. Deposita 37, 614-629.

Bowell, R. J., 1992. Supergene gold mineralogy at Ashanti, Ghana: Implications for the supergene behaviour of gold. Mineral. Mag. 56, 545-560.

Bowell, R. J., Foster, R. P., Stanley, C. J., 1990. Telluride mineralization at Ashanti gold mine, Ghana. Mineral. Mag. 54, 617-627.

Bucci, L. A., Hagemann, S. G., Groves, D. I., Standing, J. G., 2002. The Archean Chalice gold deposit: a record of complex, multistage, high-temperature hydrothermal activity and gold mineralization associated with granitic rocks in the Yilgarn Craton, Western Australia. Ore Geol. Rev. 19, 23-67.

Brown, K. L.,1986. Gold deposition from geothermal discharges in New Zealand. Econ. Geol., 81, 979-986 .

Caddey, S. W., Bachman, R. L., Campbell, T. J., Reid, R. R., Otto, R. P., 1991. The Homestake Gold Mine, An Early Proterozoic Iron-Formation-Hosted Gold Deposit, Lawrence County, South Dakota. Geology and Resource of Gold in the United States, pp. J1-J67.

Cameron, E. M., Hattori, K., 1985. The Hemlo gold deposit, Ontario: A geochemical and isotopic study. Geochim. Cosmochim. Acta 49, 2041-2050.

Cocke, H. A., Mauk, J. L., Rabone, D. C., 2013. The origin of Ag–Au–S–Se minerals in adularia-sericite epithermal deposits: constraints from the Broken Hill sdeposit, Hauraki Goldfield, New Zealand. Miner Deposita, 48, 249-266.

Chryssoulis, S.L., 2001. Using mineralogy to optimize gold Recovery by flotation. JOM, 53, 48-50.

Desborough, G. A., Heidel, R. H., Raymond, W. H., Tripp, J., 1971. Primary distribution of silver and copper in native gold from six deposits in the Western United States. Mineral. Deposita 6, 321-334.

Espi, J. O., Hayashi, K. I., Komuro, K., Murakami, H., Kajiwara, Y., 2007. Geology, Wall-rock Alteration and Vein Paragenesis of the Bilimoia Gold Deposit, Kainantu Metallogenic Region, Papua New Guinea. Resour. Geol. 57, 249-268.

Etoh, J., Izawa, E., Taguchi, S., 2002. A Fluid Inclusion Study on Columnar Adularia from the Hishikari Low-sulfidation Epithermal Gold Deposit, Japan. Resour. Geol. 52, 73–78.

Fisher, N. H., 1945. The fineness of gold, with special reference to the Morobe gold field, New Guinea. Econ. Geol. 40, 449-495.

Frimmel, H. E., Gartz, V. H., 1997. Witwatersrand gold particle chemistry matches model of metamorphosed, hydrothermally altered placer deposits. Mineral. Deposita 32, 523-530.

Frimmel, H. E., Hallbauer, D. K., Gartz, V. H., 1999. Gold mobilizing fluids in the Witwatersrand Basin: composition and possible sources. Mineral. Petrol. 66, 55–81.

Gammons, C. H., Barnes, H.L., 1989. The solubility of Ag_2S in near-neutral aqueous sulfide solutions at 25 to 300°C. Geochim. Cosmochim. Acta 53, 279-290.

Gammons, C.H., Williams-Jones, A .E., 1995. The solubility of Au-Ag alloy + AgCl in HCl/NaCl solutions at 300°C: New data on the stability of Au (1) chloride complexes in hydrothermal fluids. Geochim. Cosmochim. Acta 59, 3453-3468.

Gan, X. C.,1996. U-Pb age dating on zircons from volcanic rocks of the Proterozoic and Archean in southern China. Geochimica, 25,112–120 (in Chinese with English abstract).

Gan, S. F., Qiu, Y. M., Yang H. Y. and Van Reenen, D. D., 1994. The Hadamengou mine: A Typical gold deposit in the Archean granulite facies terrane of the north China Craton. Inter. Geol. Rev. 36, 850-866.

Gu, X.X., Schulz, O., Vavtar, F., Liu, J.M., Zheng, M.H. and Fu, S.H., 2007.

Rare earth element geochemistry of the Woxi W-Sb-Au deposit, Hunan Province, South China. Ore Geol. Rev., 31, 319-336.

Gurevich, V.M., Gavrichev, K.S., Osadchii, E.G., Tyurin, A.V., Ryumin, M.A., 2011. Heat capacity and thermodynamic functions of petrovskaite (AgAuS) at 0–583 K and mineral equilibria in the Ag–Au–S system. Geochem. Int. 49, 422-428.

Green, A. H., Donnelly, T. H., Jahnke, F. M., Keays, R.R., 1982. Evolution of gold-bearing veins in dykes of the Woods Point dyke swarm, Victoria. Mineral. Deposita 17, 175-192.

Greffie, C., Bailly, L., Milesi, J. P., 2002 Supergene alteration of primary ore assemblages from low-sulfidation Au–Ag epithermal deposits at Pongkor, Indonesia, and Nazareno, Peru. Econ. Geol. 97, 561-571.

Harris D.C. (1986) Minerals in the Main Hemlo gold deposit, Ontario. Current Res., art A, Geol. Surv. Can., pp. 86-1A: 49-54.

Hayashi, K., Ohmoto, K., 1991. Solubility of gold in NaCl- and H_2S-bearing aqueous solutions at 250-350°C. Geochim. Cosmochim. Acta 55, 2111-2126.

Heinrich, C.A., Pettke, T., Halter, W.E., Aigner-Torres, M., Audtetat, A., Gunther, D., Hattendoer, B., Bleiner, D., Guillong, M. and Horn, I., 2003. Quantitative multi-element analysis of minerals, fluid and melt inclusions by laser-ablation inductively-coupled-plasma mass-spectrometry. Geochim. Cosmochim. Acta, 67, 3473-3496.

Henley, R. W., Truesdell, A. H., Barton, P. B., 1984. Metals in hydrothermal fluids, Fluid-mineral equilibria in hydrothermal systems. Reviews in Econ. Geol., 1, 115-127.

Hu, H., Wang, R. C., Lu, J. J., Liu, G. H., 2001. Mineral association, chemical composition and genetic significance of Skarn gold deposit in the Shizishan Orefield, Tongling Area, Anhui Province. Mineral Deposit, 20, 86-98. (in Chinese with English abstract)

Huston, D. L., Large, R. R., 1989. A chemical model for the concentration of gold in volcanogenic massive sulphide deposits. Ore Geol. Rev. 4, 171-200.

Huston, D.L., Bottrill, R.S., Creelman, R.A., Zaw, K., Ramsden, T.R., 1992. Geological and geochemical controls on the mineralogy and grain size of gold-bearing phases, eastern Australian volcanic-hosted massive sulphide deposits. Econ. Geol. 87, 542-563.

Izawa, E., Urashima, Y., Ibaraki, K., Suzuki, R., Yokoyama, T., Kawasaki, K., Koga, A., Taguchi, S., 1990. The Hishikari gold deposit: high-grade epithermal veins in Quaternary volcanics of southern Kyushu, Japan. J. Geochem. Explor. 36, 1-56.

Johnson, J.W., Oelkers, E.H., Helgeson, H.C., 1992. SUPCRT-92. Comput. Geosci. 18 (7), 899-947.

Kajiwara, Y., 1971. Sulfur isotope study of the Kuroko-ores of the Shakanai No.1 deposits, Akita Prefecture, Japan. Geochem. J. 4, 157-181.

Koga, A. (1961) Gold in Beppu thermal springs. J. Chem. Soc. Japan, 82, 1476-1478 (in Japanese with English abstract).

Kreuzer, O. P., 2006. Textures, paragenesis and wall-rock alteration of lode-gold deposits in the Charters Towers district, north Queensland: implications for the conditions of ore formation. Mineral. Deposita 40, 639-663.

Kreuzer, O. P., Blenkinsop, T.G., Morrison, R.J., Peters, S. G., 2007. Ore controls in the Charters Towers goldfield, NE Australia Constraints from geological, geophysical and numerical analyses. Ore Geol. Rev. 32, 37-80.

Krupp, R. E., Weiser, T., 1992. On the stability of gold-silver alloys in the weathering environment. Mineral. Deposita 27, 268-275.

Landtwing, M. R., Furrer, C., Redmond, P. B., Pettke, T., Guillong, M., Heinrich, C. A., 2010. The Bingham Canyon Porphyry Cu-Mo-Au Deposit. III. Zoned Copper-Gold Ore Deposition by Magmatic Vapor Expansion. Econ. Geol. 105, 91-118.

Lang, J. R., Eastoe, C. J., 1988. Relationships between a porphyry Cu-Mo deposit, base and precious metal veins and Laramide intrusions, Mineral Park, Arizona. Econ. Geol. 83, 551-567.

Lawrance, L. M., Griffin, B. J., 1994. Crystal features of supergene gold at Hannan South, Western Australia. Mineral. Deposita 29, 391-398.

Lu, H. Z., 2000. High temperature, salinity and high concentrated ore metal magmatic fluids: an example from Grasberg Cu-Au porphyry deposit. Acta

Petrol. Sin. 16, 465-472.

Luo, X. L., Zhong, D.Q. and Li, G.S., 1996. Geology of the Woxi-type stratabound gold deposits in Hunan Province. Seismic Press, 313 pp. (in Chinese with English abstract).

Maeda, H., 1998. Relationships between Volcanism, Hydrothermal Alteration and Epithermal Gold-Silver Mineralization in the Muka Mine Area in the Kitami Metallogenic Province, Hokkaido, Japan. Resour. Geol. 48, 197-208.

Maglambayan, V. B., Ishiyama, D., Mizuta, T., Akira, I., Ishikawa, Y., 1998. Geology, Mineralogy, and Formation Environment of the Disseminated Gold-Silver Telluride Bulawan Deposit, Negros Occidental, Philippines. Resour. Geol. 48, 87-104.

Mariam, M. G., Groves, D. I., McNaughton, N. J., Mikucki, E. J., Vearncombe, J. R., 1993. Archaean Au-Ag mineralisation at Racetrack, near Kalgoorlie, Western Australia: a high crustal-level expression of the Archaean composite lode-gold system. Mineral. Deposita 28, 375-387.

McInnes, B. I. A., McBride, J. S., Evans,N. J., Lambert, D. D., Andrew, A. S., 1999. Osmium isotope constraints on ore metal recycling in subduction zones. Science 286, 512-516.

Meinert, L. D., Hefton, K. K., Mayes, D., Tasiran, I., 1997. Geology, zonation, and fluid evolution of the Big Gossan Cu-Au skarn deposit, Ertsberg district, Irian Jaya. Econ. Geol. 92, 509-534.

Mernagh, T. P., Heinrich, C. A. and Mikucki, E. J., 2004. Temperature

gradients recorded by fluid inclusions and hydrothermal alteration at the Mount Charlotte gold deposit, Kalgoorlie, Australia. Can. Mineral. 42, 1383-1 404.

Minoru, K., Hodge, V., Goldberg, E. D. and Bertine, K.,1988. Gold in seawater: A conservative view. Appl. Geochem., 3, 237-241

Moritz, R., 2006. Fluid salinities obtained by infrared microthermometry of opaque minerals: Implications for ore deposit modeling — A note of caution. J. Geochem. Explor. 89, 284-287.

Morrison, G. W., Rose, W. J., Jaireth, S., 1991. Geological and geochemical controls on the silver content (fineness) of gold in gold-silver deposits. Ore Geol. Rev. 6, 333-364.

Mueller, A. G., 2007. Copper-gold endoskarns and high-Mg monzodiorite-tonalite intrusions at Mt. Shea, Kalgoorlie, Australia: implications for the origin of gold-pyrite-tennantite mineralization in the Golden Mile. Mineral. Deposita 42, 737-769.

Mueller, A. G., Muhling, J. R., 2013. Silver-rich telluride mineralization at Mount Charlotte and Au–Ag zonation in the giant Golden Mile deposit, Kalgoorlie, Western Australia. Mineral. Deposita 48, 295-311.

Mueller, A. G., Lawrance, L. M., Muhling, J., 2012. Mineralogy and PTX Relationships of the Archean Hannan South Au-Cu (Co-Bi) Deposit, Kalgoorlie, Western Australia: Thermodynamic Constraints on the Formation of a Zoned Intrusion-Related Skarn. Econ. Geol. 107, 11-24.

Muller, D., Kaminski, K., Uhlig, S., Graupner, T., Herzig, P. M., Hunt, S., 2002. The transition from porphyry- to epithermal-style gold mineralization at Ladolam, Lihir Island, Papua New Guinea: a reconnaissance study. Mineral. Deposita 37, 61-74.

Murakami, H., Seo, J. H., Heinrich, C. A., 2010. The relation between Cu/Au ratio and formation depth of porphyry-style Cu-Au±Mo deposits. Mineral. Deposita 45, 11-21.

Muir, T.L., 2002. The Hemlo gold deposit, Ontario, Canada: principal deposit characteristics and constraints on mineralization. Ore Geol. Rev. 21, 1-66.

Nair, N. G. K., Santosh, M., Mahadevan, R., 1987. Lateritisation as a possible contributor to gold placers in Nilambur Valley, Southwest India. Chem. Geol. 60, 309-315.

NRM, department of Natural Resources and Mines geological survey of Queensland (2012) Queensland's significant mineral mines, advanced mineral projects and new intersections. http://mines.industry.qld.gov.au/assets/coal-pdf/minerals_2012.pdf.

O'Dea, T. R., 1980. Gold mineralization at Porgera, Papua New Guinea. Proc. Australasian Inst. Mining Metall. Conf. pp. 9–24

Pal'yanova, G. A., 2008. Physicochemical modeling of the coupled behavior of gold and silver in hydrothermal processes: Gold fineness, Au/Ag ratios and their possible implications. Chem. Geol. 255, 399-413.

Pal'yanova, G. A., Kolonin, G. R., 2007. Geochemical Mobility of Au and Ag

during Hydrothermal Transfer and Precipitation: Thermodynamic Simulation. Geochem. Int. 45, 744-757.

Palyanova, G. A., Savva, N. E., 2008. Some Sulfides of Gold and Silver: Composition, Mineral mineral Assemblage, and Conditions of Formation. Theor. Found. Chem. En. 42, 749-761.

Palyanova, G.A., Kokh, K.A., Seryotkin, Y. V., 2011. Formation of gold and silver sulfides in the system Ag-Au-S. Russ. Geol. Geophys. 52, 443-449

Pan, Y., Fleet, M. E., 1995. The late Archean Hemlo gold deposit, Ontario, Canada: a review and synthesis. Ore Geol. Rev. 9, 455-488.

Petersen, S., Herzig, P. M., Hannington, M. D., Jonasson, I. R., 2002. Submarine gold mineralization near Lihir Island, New Ireland fore-arc, Papua New Guinea. Econ. Geol. 97, 1795-1813.

Peng, B., and Robert F., 2004. Nd-Sr-Pb isotopic constraints on metal and fluid sources in W-Sb-Au mineralization at Woxi and Liaojiaping (Western Hunan, China). Mineral. Deposita, 39, 313–327.

Prendergast, K., Clarke, G. W., Pearson, N. J., Harris, K., 2005. Genesis of Pyrite-Au-As-Zn-Bi-Te Zones associated with Cu-Au Skarns: evidence from the Big Gossan and Wanagon Gold Deposits, Ertsberg District, Papua, Indonesia. Econ. Geol. 100, 1021-1050.

Qian, J., Chen, H., Meng, Y., 2011. Geological characteristics of the Sizhuang gold deposit in the region of Jiaodong, Shandong Province - A study on tectono-geochemical ore prospecting of ore deposits. Chin. J. Geochem. 30,

539-553.

Rae, A. J., Cooke, D. R., Brown, K. L., 2011. The trace metal chemistry of deep geothermal water, Palinpinon geothermal field, Negros island, Philippines: Implications for precious metal deposition in epithermal gold deposits. Econ. Geol. 106, 1425-1446.

Rasmussen, B., Mueller, A. G. and Fletcher, L. R., 2009. Zirconolite and xenotime U-Pb age constraints on the emplacement of the Golden Mile Dolerite sill and gold mineralization at the Mt Charlotte mine. Contrib. Mineral Petrol. 157, 559-572.

Reid, A. M., le Roex, A. P., Minter, W. E. L., 1988. Composition of gold grains in the Vaal Placer, Klerksdorp, South Africa. Mineral. Deposita 23, 211-217.

Richards, J. P., 1990. Petrology and geochemistry of alkalic intrusives at the Porgera gold deposit, Papua New Guinea. J. Geochem. Explor. 35, 141-199.

Richards, J. P., McCulloch, M. T., Chappell, B. W., Kerrich, R., 1991. Sources of metals in the Porgera gold deposit, Papua New Guinea: Evidence from alteration, isotope, and noble metal geochemistry. Geochim. Cosmochim. Acta 55, 565-580.

Rubin, J. N., Kyle, J. R., 1997. Precious metal mineralogy in porphyry-, skarn-, and replacement-type ore deposits of the Ertsberg (Gunung Bijih) District, Irian Jaya, Indonesia. Econ. Geol. 92, 535-550.

Rusk, B. G., Reed, M. H., Dilles, J. H., 2008. Fluid inclusion evidence for

magmatic-hydrothermal fluid evolution in the porphyry copper-molybdenum deposit at Butte, Montana. Econ. Geol. 103,307-334.

Rusk, B. G., Reed, M. H., Dilles, J. H., Klemm, L. M., Heinrich, C. A., 2004. Magmatic fluid evolution from an ancient magmatic-hydrothermal system: The porphyry copper-molybdenum deposit, Butte, MT. Chem. Geol. 210, 173-199

Saager, R., Esselaar, P. A., 1969. Factor analysis of geochemical data from the basal reef, Orange Free State goldfield, South Africa. Econ. Geol. 64, 445-451.

Santosh, M., Philip, R., Jacob, M. K., Omana, P. K., 1992. Highly pure placer gold formation in the Nilambur Valley, Wynad Gold Field, southern India. Mineral. Deposita 27, 336-339.

Sasaki, M., Iizasa, K., Sawaki, T., 1995. Characteristics of gases in fluid inclusions from the Nurukawa kuroko deposit and submarine sulfide deposits of the Izu-Ogasawara arc, Japan. Resour. Geol. 45, 1-10.

Sato, J., 1974. Ores and ore minerals from the Shakanai mine, Akita Prefecture, Japan. Mining Geology Special Issue 6, 323-335.

Seo, J. H., Guillong, M., Heinrich, C. A., 2009. The role of sulfur in the formation of magmatic-hydrothermal copper-gold deposits. Earth Planet. Sci. Lett. 282, 323-328

Shikazono, N., Shimizu, M., 1987. The Ag/Au ratio of native gold and electrum and the geochemical environment of gold vein deposits in Japan. Mineral.

Deposita 22, 309-314.

Sheets, R.W., Craig, J.R., Bondar, R.J., 1995 Composition and occurrence of electrum at the Morning Star deposit, San Bernandino County, California: evidence for remobilization of gold and silver, Can. Mineral. 33, 137-151.

Simmons, S. F., Brown, K. L., 2006. Gold in magmatic hydrothermal solutions and the rapid formation of a giant ore deposit. Science 314, 288-291.

Simmons, S. F., Brown, K. L., 2007. The flux of gold and related metals through a volcanic arc, Taupo volcanic zone, New Zealand: Geol., 35, 1099-1102.

Singer, D. A., Berger, V.I., Moring, B. C., 2005. Porphyry copper deposits of the world: database, map, and grade and tonnage models. U.S. Geological Survey, Open File Report 2005-1060. http://pubs.usgs.gov/of/2005/1060/.

Spycher, N.F., Reed, M.H., 1989. Evolution of a broad lands-type epithermal ore fluid along alternative P-T paths: implications for the transport and deposition of base, precious and volatile metals. Econ. Geol. 84, 328-359.

Tang, X. X., Huang, J. Z., and He, K. X., 1994. Geology and geochemistry of the Banxi Group in Hunan province, China. China Regional Geol., 1, 65–71(in Chinese with English abstract).

Tanimura, S., Date, J., Takahashi, T., Ohmoto, H., 1983. Geologic setting of the kuroko deposits, Japan. Part II. Stratigraphy and structure of the Hokuroku district. Econ. Geol. Monogr. 5, 24-38.

Tagirov, B. R., Baranova, N. N., Zotov, A. V., Schott, J., Bannykh, L.N., 2006. Experimental determination of the stabilities of $Au_2S_{(cr)}$ at 25 °C and

$Au(HS)_2^-$ at 25-250 °C. Geochim. Cosmochim. Acta 70, 3689-3701.

Ulrich, T., Günther, D., Heinrich, C. A., 1999. Gold concentrations of magmatic brines and the metal budget of porphyry copper deposits. Nature 399, 676-679.

Ulrich, T., Günther, D., Heinrich, C. A., 2002. The evolution of a porphyry Cu-Au deposit, based on LA-ICP-MS analysis of fluid inclusions: Bajo de la Alumbrera, Argentina. Econ. Geol. 97, 1889-1920.

Uzunlar, N., Paterson, C. J., Lisenbee, A. L., 2010. Tertiary Epithermal to Mesothermal Porphyry-Related Au-Ag Mineralization in the Homestake Mine, Lead, South Dakota. Rocky Mountain-62nd Annual Meeting, Paper No. 8-5.
https://gsa.confex.com/gsa/2010RM/finalprogram/abstract_172053.htm

Wang, J. Z., Li, J. W., Zhao, X. F., Ma, C. Q., Qu, W. J., Du, A. D., 2008. Re-Os dating of pyrrhotite from the Chaoshan gold skarn, eastern Yangtze Craton, eastern China. Int. Eol. Rev. 50, 392-406.

White, J. L., Orr, R. L., Hultgren, R., 1957. Thermodynamic properties of silver-gold alloys. Acta Metall. 5, 747-760.

Wolfram, S., 1991. Mathematica a system for doing mathematics by computer. Second editions. Addison-Wesley, New York. 961 pp.

Yamada, R., Suyama, T., Ogushi, O., 1987. Gold-bearing siliceous ore of the Nurukawa kuroko deposit, Akita prefecture, Japan. Mining Geology, 37, 109-118.

Yang, X. N., Xu, Z. W., Gao, G., Lu, X. C., Lu, S. M., Li, H. Y., 2008. Fluid inclusion studies of the Chaoshan gold deposit in Tongling, Anhui Province, China. Acta Petrol. Sin. 24, 1889-1899. (in Chinese with English abstract)

Yang, S.X. and Blum, N., 1999a. A fossil hydrothermal system or a source-bed in the Madiyi Formation near the Xiangxi Au–Sb–W deposit, NW Hunan, PR China. Chem. Geol., 155, 151–169.

Yang, S.X. and Blum, N., 1999b. Arsenic as an indicator element for gold exploration in the region of the Xiangxi Au–Sb–W deposit, NW Hunan, PR China. J. Geochem. Explor., 66 441–456.

Zaw, K., Large, R. R., 1992. The precious metal-rich, South Hercules mineralization, western Tasmania; a possible subsea-floor replacement volcanic-hosted massive sulfide deposit. Econ. Geol. 87, 931-952.

Zaw, K., Large, R. R., 1996. Petrology and geochemistry of sphalerite from the Cambrian VHMS deposits in the Rosebery-Hercules district, western Tasmania: Implications for gold mineralization and Devonian metamorphic-metasomatic processes. Miner. Petrol. 57, 97-118.

Zaw, K., Huston, D. L., Large, R. R., 1999. A chemical model for the Devonian remobilization process in the Cambrian volcanic-hosted massive sulfide Rosebery deposit, western Tasmania. Econ. Geol. 94, 529-546.

Zhai, W., Sun, X., Sun, W., Su, L., He, X., Wu, Y., 2009. Geology, geochemistry, and genesis of Axi: A Paleozoic low-sulfidation type epithermal gold deposit in Xinjiang, China. Ore Geol. Rev. 36, 265-281.